

Three-Dimensional Structure and Temporal Evolution of Submesoscale Thermohaline Intrusions in the North Pacific Subtropical Frontal Zone

A. Y. SHCHERBINA, M. C. GREGG, M. H. ALFORD, AND R. R. HARCOURT

Applied Physics Laboratory, University of Washington, Seattle, Washington

(Manuscript received 29 September 2009, in final form 5 April 2010)

ABSTRACT

Four instances of persistent intrusive deformation of the North Pacific Subtropical Front were tagged individually by a Lagrangian float and tracked for several days. Each feature was mapped in three dimensions using repeat towed observations referenced to the float. Isohaline surface deformations in the frontal zone included sheetlike folds elongated in the alongfront direction and narrow tongues extending across the front. All deformations appeared as protrusions of relatively cold, and fresh, water across the front. No corresponding features of the opposite sign or isolated lenslike structures were observed. The sheets were $O(10)$ m thick, protruded about 10 km into the warm saline side of the front, and were coherent for 10–30 km along the front. Having about the same thickness and cross-frontal extent as the sheets, tongues extended less than 5 km along the front. All of the intrusions persisted as long as they were followed, several days to one week. Their structures evolved on both inertial (23 h) and subinertial (~ 10 days) time scales in response to differential lateral advection. The water mass surrounding the intrusions participated in gradual anticyclonic rotation as a part of a mesoscale meander of the subtropical front. The intrusions may be interpreted as a manifestation of three-dimensional submesoscale turbulence of the frontal zone, driven by the mesoscale. Absence of large features of the opposite sign may be indicative of the asymmetry of the underlying dynamics.

1. Introduction

a. Background and motivation

The three-dimensional structure and evolution of thermohaline intrusions remain elusive in spite of many observations, following the discovery of laterally coherent temperature inversions near the Gulf Stream by Spilhaus (1940). Based on thousands of bathythermograph records in the North Pacific, Roden (1964) found temperature inversions to be common throughout the North Pacific. Remarking on apparent differences in the origin of low- and high-latitude inversions, Roden pointed out that the strongest tropical and subtropical features are associated with water mass boundaries, “jetlike currents,” and the equator. He further speculated that the tropical inversions “may be due to turbulence.” Conductivity–temperature–depth (CTD) casts showed these temperature inversions to be hydrostatically stable due to salinity stratification (Roden 1964; Stommel and Fedorov 1967). Microstructure profiling resolved small

“staircases” within many temperature–salinity inversions, composed of relatively homogeneous $O(1$ m) thick layers separated by sharp $O(1$ cm) thick interfaces (Gregg and Cox 1972). Such staircase structures have also been observed beneath the temperature–salinity maxima in the Gulf Stream (Gregg 1980), although less frequently than in the temperature inversions above these maxima. Sections of CTD profiles frequently feature intrusions sloping across density surfaces (e.g., Fedorov 1978; Gregg and McKenzie 1979), but we are aware of only one previous three-dimensional open-ocean mapping effort (Gregg 1980).

As noted by Roden (1964) and Stommel and Fedorov (1967), hydrostatically stable temperature–salinity inversions in the subtropics can result only from differential advection. From the singular nature of temperature–salinity staircases commonly observed within the inversions, it has been inferred that anomalies in stratification produced by double diffusion drive the necessary lateral advection. Moreover, profiles near fronts often contain multiple inversions extending over vertical intervals of tens or hundreds of meters (Joyce 1977), strongly resembling the structures produced in a laboratory tank when a disturbance was introduced into a diffusively unstable

Corresponding author address: A. Y. Shcherbina, APL-UW, 1013 NE 40th St., Seattle, WA 98105.
E-mail: ashcherbina@apl.washington.edu

water column (Turner and Chen 1974). Ruddick and Richards (2003) and Ruddick and Kerr (2003) reviewed the extensive literature on observations and theory of intrusions, focusing on their links to double diffusion.

Double-diffusive and the closely related McIntyre instabilities (McIntyre 1970), however, are not the only potential sources of interleaving in the ocean. Frontal intrusions may also be generated by three-dimensional ageostrophic turbulence and linked directly to frontogenesis (Klein et al. 1998). Recent studies have focused on oceanic submesoscale dynamics, the spectral transition between the mesoscale (tens to hundreds of kilometers), where most of the ocean's energy resides, and the microscale (millimeters to meters), where the actual dissipation of energy is thought to occur (McWilliams et al. 2001; Thomas et al. 2008; Smith and Ferrari 2009). Unlike mesoscale turbulence, submesoscale flow is essentially three-dimensional, so the vertical velocities associated with these features may be strong enough to have a local effect on both lateral and vertical fluxes of heat, salt, nutrients, and other tracers (Mahadevan et al. 2008; Thomas et al. 2008). Indirect evidence of vertically sheared submesoscale exchange is occasionally observed as intrusions or interleaving at the edges of mesoscale features (Tang et al. 1985; Schmitt et al. 1986; Armi et al. 1989; Hitchcock et al. 1994). It is a compelling possibility that such interleaving is the three-dimensional expression of submesoscale turbulence, conceptually similar to the complex structure of streaks and filaments revealed by surface observations. Generation of density-compensated thermohaline filaments with complex vertical structure as a result of lateral stirring of large-scale thermohaline gradients by geostrophic turbulence has been demonstrated in quasigeostrophic modeling by Smith and Ferrari (2009).

b. Experiment objective

To investigate the three-dimensional structure and evolution of frontal interleaving, an intensive field survey was conducted in the subtropical frontal zone (STFZ) north of Hawaii in July 2007, the STF07 experiment. The experiment focused on the outer edge of a mesoscale meander of the STFZ, clearly identified as a relatively warm filament in sea surface temperature imagery (Fig. 1). Within the filament, two thermohaline fronts (referred to as F1 and F2) were the apparent region of generation for interleaving features.

This study addressed operational and scientific questions:

- 1) Can submesoscale frontal intrusions be mapped in three dimensions and followed over a period of time? Having only one ship available, our approach

was predicated on 1) using satellite sea surface temperature (SST) images as guides to frontal structures in the thermocline and 2) surveying the immediate vicinity of the features of interest that were tracked using a neutrally buoyant subsurface Lagrangian float.

- 2) What three-dimensional shapes and spatiotemporal scales characterize intrusions in the front? Do they have highly variable shapes and scales or are they relatively uniform?
- 3) Where do intrusions occur on the front in relation to velocity and shear as well as to temperature and salinity? Are there preferred locations or relations to velocity, for example, near-inertial shear? Do some parts of the front lack intrusions? Do intrusions occur as transient deformations or do they detach from the front?
- 4) What processes generate the intrusions? Are the driving mechanisms internal to the intrusions (e.g., double-diffusive instability) or external (e.g., the submesoscale turbulence cascade)?
- 5) What diapycnal and lateral fluxes result from these features and where?

A few of these questions were addressed in a preceding paper (Shcherbina et al. 2009, hereafter SGAH09) that focused on the large-scale statistics of interleaving derived from the fields of diapycnal spiciness curvature. In particular, it was reported that the intrusions were most prevalent near the two curved thermohaline fronts located at the periphery of an anticyclonic meander in the STFZ. The vertical and cross-frontal scales of the intrusions were on the order of 10 m and 5 km, respectively. The slopes of these features were highly variable and typically not consistent with double-diffusive intrusion origin. Here, we take a phenomenological approach complementary to SGAH09 and describe three-dimensional deformation of salinity fields associated with several prominent intrusions.

c. Tracking and mapping frontal intrusions

Tracking open-ocean frontal intrusions presents unique operational challenges and, to our knowledge, has never been done prior to this experiment. Even though intrusions are embedded in the fluid and follow its motion to a certain extent, they are not truly Lagrangian because their existence and location inherently depend on the difference in the advection of the neighboring layers. Owing to the practical limitations on the extent of a single-vessel survey in space–time, a quasi-Lagrangian observation strategy was adopted. With this approach, the evolution of intrusions was investigated using a series of three-dimensional surveys in the reference frame following a tracked Lagrangian float (D'Asaro 2003).

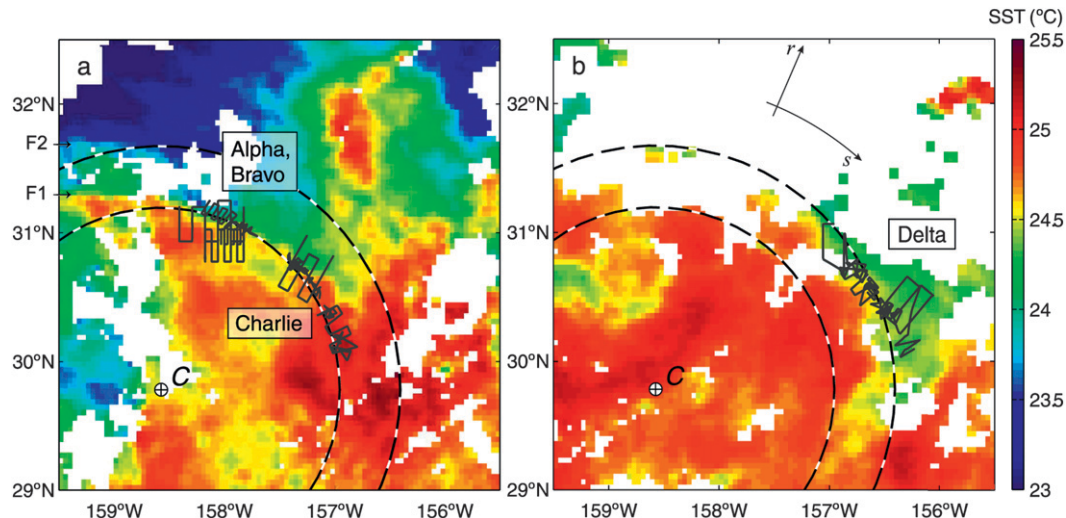


FIG. 1. SWIMS survey lines for the periods (a) 13–21 Jul and (b) 21–26 Jul 2007. Background shows sea surface temperatures on (a) 7 Jul and (b) 20 Jul 2007, based on Moderate Resolution Imaging Spectroradiometer (MODIS) *Aqua* imagery (courtesy of NASA/JPL/PODAAC). Dashed lines mark the 157-km and 210-km reference circles, centered at point C. Surface expressions of two thermohaline fronts (F1 and F2) are marked in (a). Labels indicate the survey segments (see Fig. 2); note that surveys Alpha and Bravo are separated in time rather than geographically. Orientation of the coordinate system (*s*, *r*) is shown in (b).

This paper focuses on 20 days of the STF07 experiment (7–26 July 2007) when several frontal intrusions were tracked and measured extensively. The time line of the cruise, listing the instrument deployments, is shown in Fig. 2. It is further subdivided into four cruise segments—Alpha, Bravo, Charlie, and Delta—corresponding to the distinct regions of the frontal zone surveyed.

The following strategy was used to locate and track the intrusions within the front.

- 1) The general location of the front was identified using the satellite sea surface temperature data.
- 2) Precise location and subsurface thermohaline structure of the front was obtained using a long (~100 km) zonal tow of the Shallow Water Integrated Mapping System (SWIMS) (Klymak and Gregg 2001; Alford et al. 2005), a depth-cycling towed instrument platform.
- 3) When a section of a front with noticeable interleaving was found, a large-scale (25 km × 25 km) “radiator” grid pattern centered at the front was surveyed with SWIMS to establish the rough three-dimensional context of the observed features.
- 4) A Deep Lagrangian Float (D’Asaro 2003) was then deployed in the vicinity of the intrusion to track its general advection. Trajectory of the float advection has been charted using acoustic tracking and shipboard velocity measurements (see appendix A).
- 5) While tracking the float for 2 to 3 days, a series of smaller radiator- and star-shaped SWIMS surveys

(~10 × 10 km) around the float and Modular Microstructure Profiler (MMP) drops were executed to map the small-scale structure and evolution of the intrusions. The patterns were intentionally distorted to compensate for the predicted water mass advection over the duration of the tow and ensure systematic sampling in the advected frame of reference.

Particular features targeted by this study were advected along the arc of a mesoscale anticyclonic meander at a rate of about 0.3 m s^{-1} , covering about 180 km per week (Fig. 1). For example, even though the Alpha and Bravo segments have similar geographic coordinates, they represent different realizations of the frontal structure due to advection. To compare observations of the water mass structure, an advected reference frame (ARF) was adopted.

July day	7	8	9	10	11	12	13	14	15	16	17	18	19	20	21	22	23	24	25	26
SWIMS	4	5	6	7	9	10	11	12	13		15	17	19	21	23	24	26	28	29	30
MMP										4										
Float					2				3		4					5				
Location	Inner front (F1)										Outer front (F2)									
Segment	“Alpha”					“Bravo”					“Charlie”					“Delta”				

FIG. 2. Time line of the experiment, showing the periods of instrument deployments (SWIMS, MMP, Float), as well as the location of the survey relative to the meander and the four cruise segments. The numbers in boxes indicate sequential designations of instrument deployments.

Mesoscale advection was predominantly tangential to a circular arc centered at $29^{\circ}47'N$, $158^{\circ}34'W$ (hereafter, point C) and aligned with the filament, as evident from shipboard ADCP observations (Fig. 3) and float deployments: in a cylindrical coordinate system with origin C, standard deviation of radial float displacement was only about 0.7 km, compared to the tangential displacements on the order of 50–100 km. ARF coordinates (s, r) essentially describe tangential arc length (clockwise) and radial distance relative to a certain water parcel being advected along the arc of the meander. The details of the ARF construction based on shipboard and float observations are given in appendix B. Comparison of ARF coordinates allowed us to identify corresponding features in different surveys.

Three-dimensional distributions of hydrographic parameters in ARF were obtained with level-by-level isopycnal mapping using the thin-plate smoothing spline technique (appendix C). Semi-Lagrangian (SL) depth z_{SL} , defined as the mean depth of a given isopycnal (Alford et al. 2005), was chosen as the working vertical coordinate to minimize the aliasing of relatively fast distortions in the thermohaline field by internal waves.

2. The 3D structure of the intrusions

a. Shapes of corrugated isohaline surfaces

Intrusions in the STFZ were manifested as corrugations in isohaline surfaces where they shoal across the F1 and F2 fronts toward the outside of the meander. In some cases (especially in Bravo and Delta segments) individual intrusions were prominent and coherent enough to motivate following them closely to investigate the details of their structure and evolution. In others (e.g., in Alpha and Charlie segments), the corrugation was weaker and less regular. Below, we present the structures that were covered in sufficient detail to be certain of their general topology. At the same time, they are representative of the range of features encountered during the survey.

Early in the cruise (segment Alpha, 5–12 July), only a few intrusions of small extent were observed. An example of a typical shape of isohaline surfaces within the front during this period is shown in Fig. 4. Despite somewhat corrugated appearance of the isohaline surfaces, no pronounced folds with salinity inversions characteristic of strong intrusions (SGAH09) were evident. The cross-frontal extent of the most prominent folds (e.g., near $s = 110$ km) did not exceed 3 km, and they did not extend downfront enough to appear on more than one cross-front section. In search of more substantial intrusions, the survey was moved upstream

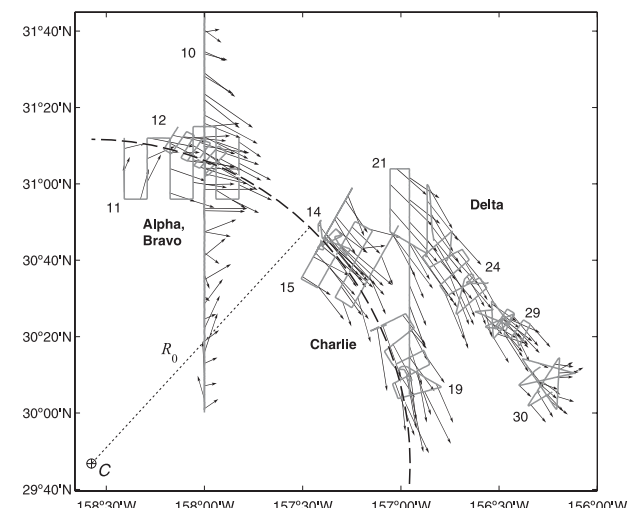


FIG. 3. Shipboard ADCP observations of mean advection velocity in the upper 100 m (arrows) from 13–26 Jul 2007; track lines are plotted in gray (only selected survey segments are shown for clarity). Dashed line marks a reference circle with radius $R_0 = 157$ km centered at point C. Numbers mark some of the SWIMS deployments. Labels indicate the four survey segments.

to the area showing a stronger sea surface temperature front in satellite imagery (Fig. 1a).

The first substantial deformation of isohaline surfaces was encountered on July 13 (Fig. 5). On the vertical profiles, the deformation had a local salinity minimum near $\sigma_\theta = 24.6\text{--}24.7 \text{ kg m}^{-3}$ (z_{SL} between 55 and 65 m). This prominent intrusion and its vicinity (segment Bravo) were targeted specifically in subsequent surveys to document its evolution over the following days (Fig. 6). Shaped like a broad sheet, it extended in the alongstream direction for $\Delta s = 30$ km from $s = -15$ to $+15$ km in the float-relative arclength coordinates, and for approximately $\Delta r = 10$ km across. The apparent gap in the intrusive sheet between $s = 1$ and 5 km may be a sampling artifact, as discussed further in appendix D. The property distributions for the “core” of the Bravo intrusion are described in section 2b. This sheetlike intrusion was observed throughout the Bravo survey 13–18 July in the same ARF vicinity and density range (Fig. 6), and possibly as late as 19 July (see Fig. 7 below). The shape and extent of the intrusion changed little during this period. Unfortunately, the small changes between the surveys could not be linked conclusively with the evolution of the feature. A mismatch could arise from the error of interpolating three-dimensional fields from nonrepeatable survey tracks. Evolution of the intrusions is further discussed in section 2d.

Segment Charlie, immediately upstream of Bravo ($s = -30$ km), was surveyed 18–21 July (Fig. 7). A hint

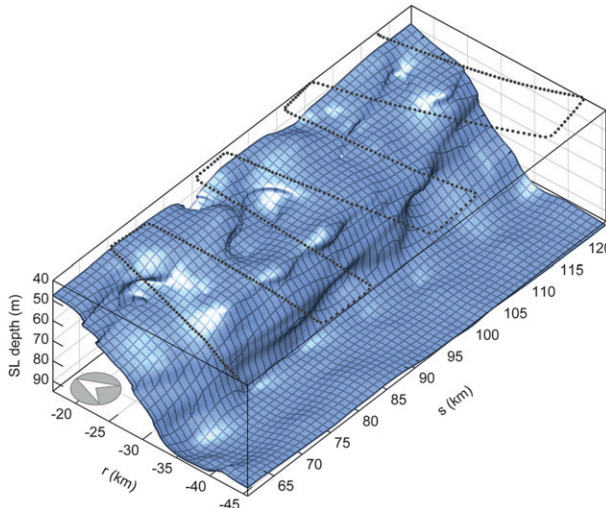


FIG. 4. A three-dimensional view of the 35.0 isohaline surface folds observed in segment Alpha (8 Jul, SWIMS deployment 6), looking northeastward from the warm and salty side of the front. Survey pattern is also shown (gray dots). the semi-Lagrangian depth is defined as the mean depth of an isopycnal (see section 1). Encircled arrow points north.

of the upstream edge of the intrusion Bravo is evident at $s = -15$ km, $z_{\text{SL}} = 70$ m, allowing cross referencing with Figs. 5 and 6. A smaller and shallower low-salinity intrusion near $r = 1$ km, $\sigma_\theta = 24.5 \text{ kg m}^{-3}$ (or $z_{\text{SL}} = 60$ m) appeared at $s \leq -20$ km and had an alongfront extent of about 20 km. Cross-front penetration of this feature was considerably less (< 2 km) than the Bravo intrusion.

Another variant of these interleaving features was observed in the vicinity of the second thermohaline front (F2) near the outer edge of the meander (segment Delta). In ARF, this area was situated about 100 km upstream and 80 km radially outward from the earlier surveys. Intrusions in this area also appear as deformations of the front, although their character is markedly different (Fig. 8). In contrast to the sheets observed earlier in Bravo and Charlie segments, intrusions in the Delta segment had elongated tongue shapes, extending cross-stream toward the center of the meander for 10–15 km. The smaller alongstream extent of these tongues was not resolved by the survey, as it was a fraction of the 5-km separation between the parallel tracks. At least two distinct tongues were surveyed—a shallow one at $\sigma_\theta = 24.1 \text{ kg m}^{-3}$, $s = -95$ km, and a deeper one at $\sigma_\theta = 24.6\text{--}24.8 \text{ kg m}^{-3}$, $s = -100$ km. The shallow tongue was situated at about 40-m depth, immediately beneath (but not extending into) the mixed layer. Both tongues persisted throughout the Delta survey. Their fragments were observed during four consecutive surveys on 23–24 July (Fig. 9), although it is difficult to

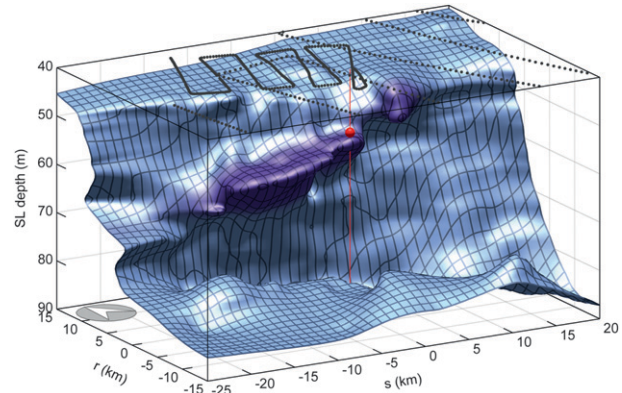


FIG. 5. A three-dimensional view of the 35.0 isohaline surface folds observed in segment Bravo (13–14 Jul, SWIMS deployments 11 and 12), looking northeastward from the warm and salty side of the front. The survey pattern is also shown (gray dots); location of the Lagrangian float deployment Bravo ($s = 0$ km, $r = 0$ km, $\sigma_\theta = 24.5 \text{ kg m}^{-3}$) is marked by a red sphere. A particularly strong fold discussed in the text is highlighted purple.

assess changes in their structure given the relatively sparse sampling.

b. Core properties

The Bravo intrusion was surveyed in great detail, allowing resolution of the complex lateral evolution pattern of hydrographic properties within its core. The core of an intrusion can be traced using the extrema of diapycnal spiciness curvature $\tau_{\sigma\sigma}$ (SGAH09). This parameter, calculated as a second derivative of spiciness with respect to potential density along a vertical profile, is an indicator of water mass interleaving: its high absolute values indicate sharp interfaces between dissimilar water masses. The lateral extent of the low-salinity intrusion core was defined as the area where the value of the associated $\tau_{\sigma\sigma}$ maximum exceeded $10 \text{ m}^3 \text{ kg}^{-1}$. Intrusion thickness was defined as the density difference between the core and the underlying negative curvature extremum. Here $\tau_{\sigma\sigma}$ was calculated from the temperature and salinity profiles low-passed with a filter with half-width of 0.1 kg m^{-3} (see SGAH09 for details). Properties of the Bravo intrusion core defined in this way are shown in Fig. 10.

The intrusion core had a shape of an elongated shallow bowl, shoaling toward either side of the front, as well as downstream. This shoaling was evident in both the depth of the core (Fig. 10a) and its density (Fig. 10b). Characteristic cross-frontal slopes of the intrusion core, determined by statistically robust plane fits to various areas of Fig. 10a, are given in Table 1.

The maximum cross-front intrusion extent of about 11 km was obtained between $s = -10$ and -5 km. This

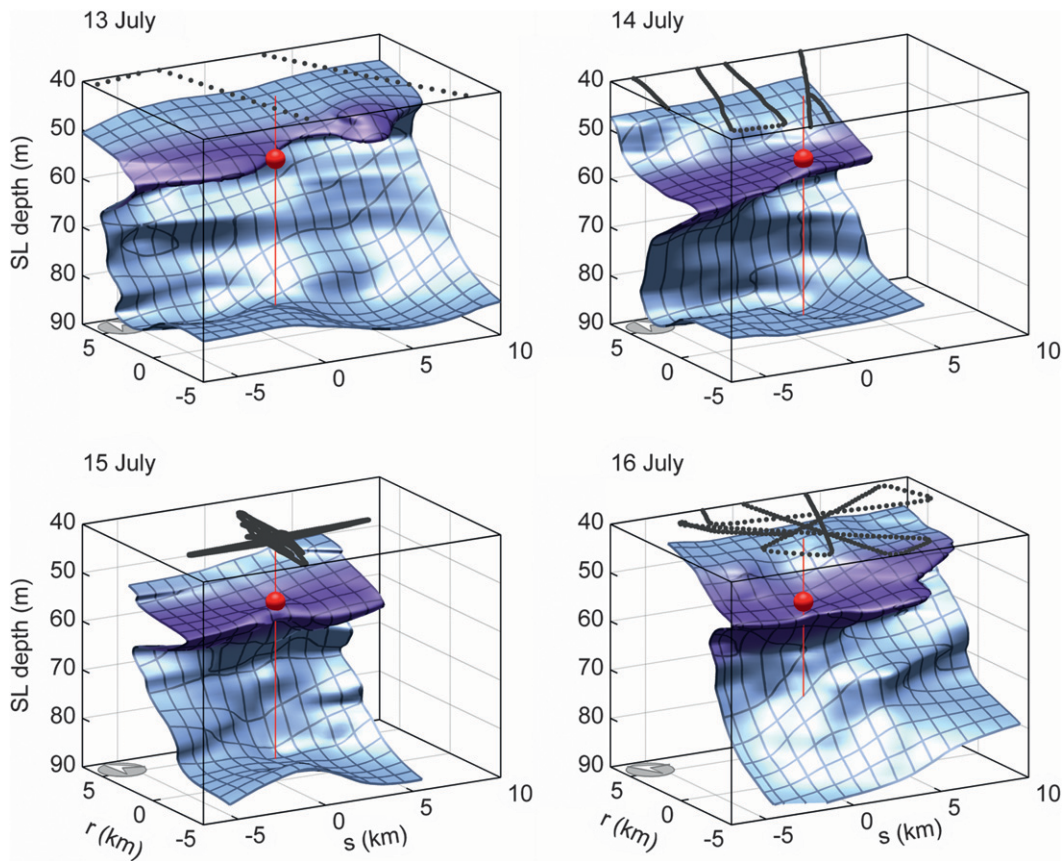


FIG. 6. Evolution of the 35.0 isohaline surface folds observed in segment Bravo 14–16 Jul (deployments 11–14) looking northeastward from the warm and salty side of the front. Survey patterns are shown with gray dots; in all cases except 15 Jul, the surveys extended beyond the area shown. The location of the Lagrangian float deployment Bravo ($s = 0 \text{ km}$, $r = 0 \text{ km}$, $\sigma_\theta = 24.5 \text{ kg m}^{-3}$) is marked by a red sphere. The particularly strong fold discussed in the text is highlighted purple.

central area was characterized by the highest values of diapycnal spiciness curvature as well (Fig. 10c). Conversely, the intrusion thickness (Fig. 10d), defined as the density difference between the core and the underlying negative curvature extremum (SGAH09), was relatively low there.

The salinity of the intrusion core (Fig. 10e) generally increased toward the intrusion tip ($r < 0$) at a rate of $(9.3 \pm 0.7) \times 10^{-6} \text{ m}^{-1}$. This increase was more pronounced near the downstream tip of the intrusion ($-5 < s < 0 \text{ km}$) where it reached $3 \times 10^{-5} \text{ m}^{-1}$, the value close to the maximum isopycnal cross-frontal salinity gradient.

Dissolved oxygen concentration within the core (Fig. 10f) monotonically decreased toward the tip of the intrusion at a rate of $(2.4 \pm 0.2) \times 10^{-5} \text{ mL L}^{-1} \text{ m}^{-1}$. The observed changes in oxygen concentration could not be attributed entirely to the effect of temperature on oxygen solubility: no more than 25% of the oxygen content

variance could be explained by the corresponding changes in temperature.

c. Area of deformation

To address the effectiveness of the lateral tracer dispersion associated with the intrusions, their scale needs to be characterized. Estimating the scale of a simple fold such as the Bravo intrusion (Fig. 5) is straightforward, but becomes progressively ambiguous as the complexity of interleaving increases, for example, multiple tongue intrusions in segment Delta. A convenient proxy can be derived using the area of isohaline surfaces A_s , which increases as the surface becomes multiply folded. We choose to disregard the vertical coordinate in calculating A_s , so its value is not affected by the tilt of the surfaces. The difference between the area of a given isohaline surface A_s and the area of its projection on the horizontal plane A_s^0 divided by two is the average area

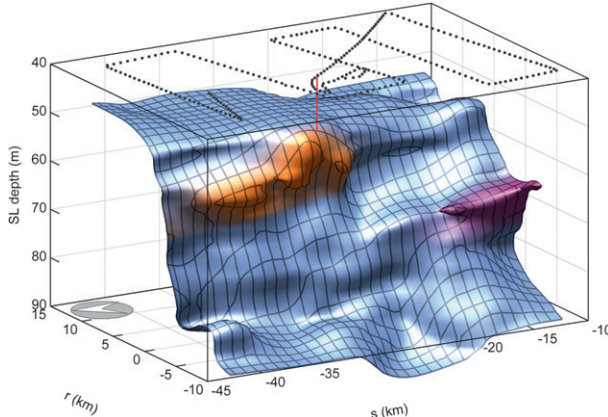


FIG. 7. A three-dimensional view of the 35.0 isohaline surface folds observed in segment Charlie 20 Jul (deployment 19), looking toward the ENE from the warm and salty side of the front. Survey pattern is also shown (gray dots). The location of the Lagrangian float deployment Charlie ($s = -28 \text{ km}$, $r = 2 \text{ km}$, $\sigma_\theta = 24.9 \text{ kg m}^{-3}$) is obscured by the surface. Two particularly strong folds discussed in the text are highlighted with purple and orange; the former is likely connected with the one highlighted in Figs. 4 and 5.

covered by folds of this isohaline surface within the domain (Fig. 11a):

$$A_s^* = (A_s - A_s^0)/2.$$

This value is a two-dimensional analog of mixing length, and will be called the area of deformation of a given isohaline. Parameterization of isosurface deformation through A_s^* is most appropriate for the surveys that encompass a single feature in its entirety (e.g., Bravo in Fig. 5). If the survey covers multiple features or, conversely, only a part of the feature (e.g., Fig. 5), A_s^* becomes sensitive to the size of the survey area. A complementary measure, the deformation ratio A_s/A_s^0 , would be more suitable in these situations. The latter, however, may be sensitive to the area of featureless margins of a survey.

Figure 11b shows the distribution of A_s^* over a range of isohaline surfaces for each of the four observation segments. The isohalines chosen to illustrate these intrusions (Figs. 4–9) were among the most deformed examples. The area of deformation in Bravo segment peaks at 200 km^2 , consistent with the $30 \text{ km} \times 10 \text{ km}$ estimate of the intrusion's extent, given its irregular shape. Confirming inspection of isohaline plots, deformations in Alpha and Charlie segments are weaker. In contrast, areas of deformation in segment Delta are substantially higher and peak at lower salinities, further highlighting the difference between the fronts F1 and F2. Deformation ratio A_s/A_s^0 of these isohalines shows similar behavior (Fig. 11c).

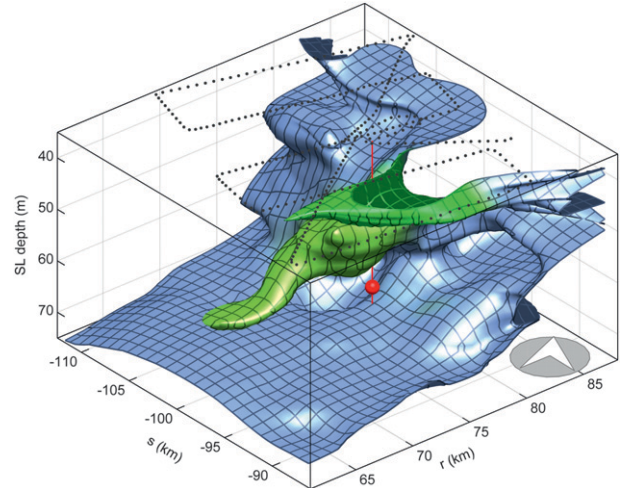


FIG. 8. A three-dimensional view of the 34.8 isohaline surface folds observed in segment Delta 23 Jul (deployment 24), looking northward from the warm and salty side of the front. Survey pattern is also shown (gray dots). The location of the Lagrangian float deployment Delta ($s = -98 \text{ km}$, $r = 76 \text{ km}$, $\sigma_\theta = 24.8 \text{ kg m}^{-3}$) is marked by a red sphere. A particularly strong multiple-tongue fold discussed in the text is highlighted green.

d. Evolution of the vertical structure

The SWIMS surveys were designed to pass repeatedly over the tracked Lagrangian float deployed in

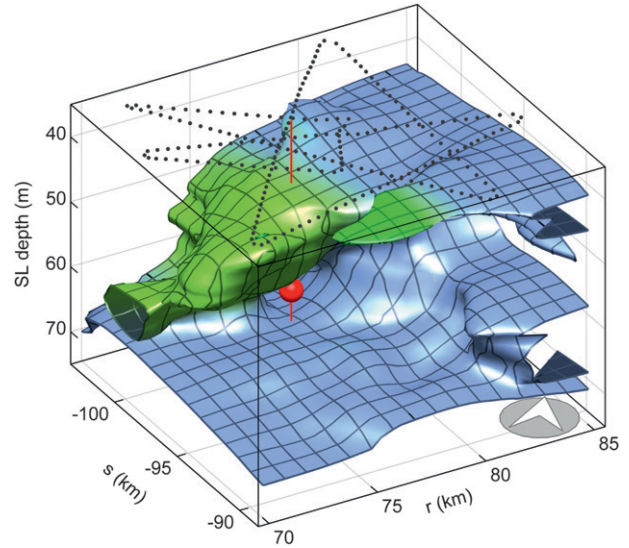


FIG. 9. A three-dimensional view of the 34.8 isohaline surface folds observed in segment Delta 24 Jul (deployment 26), looking northward from the warm and salty side of the front. Survey pattern is also shown (gray dots). The location of the fifth Lagrangian float deployment ($s = -98 \text{ km}$, $r = 76 \text{ km}$, $\sigma_\theta = 24.8 \text{ kg m}^{-3}$) is marked by a red sphere. A particularly strong multiple-tongue fold discussed in the text is highlighted green; this feature is likely related to the one highlighted in Fig. 8.

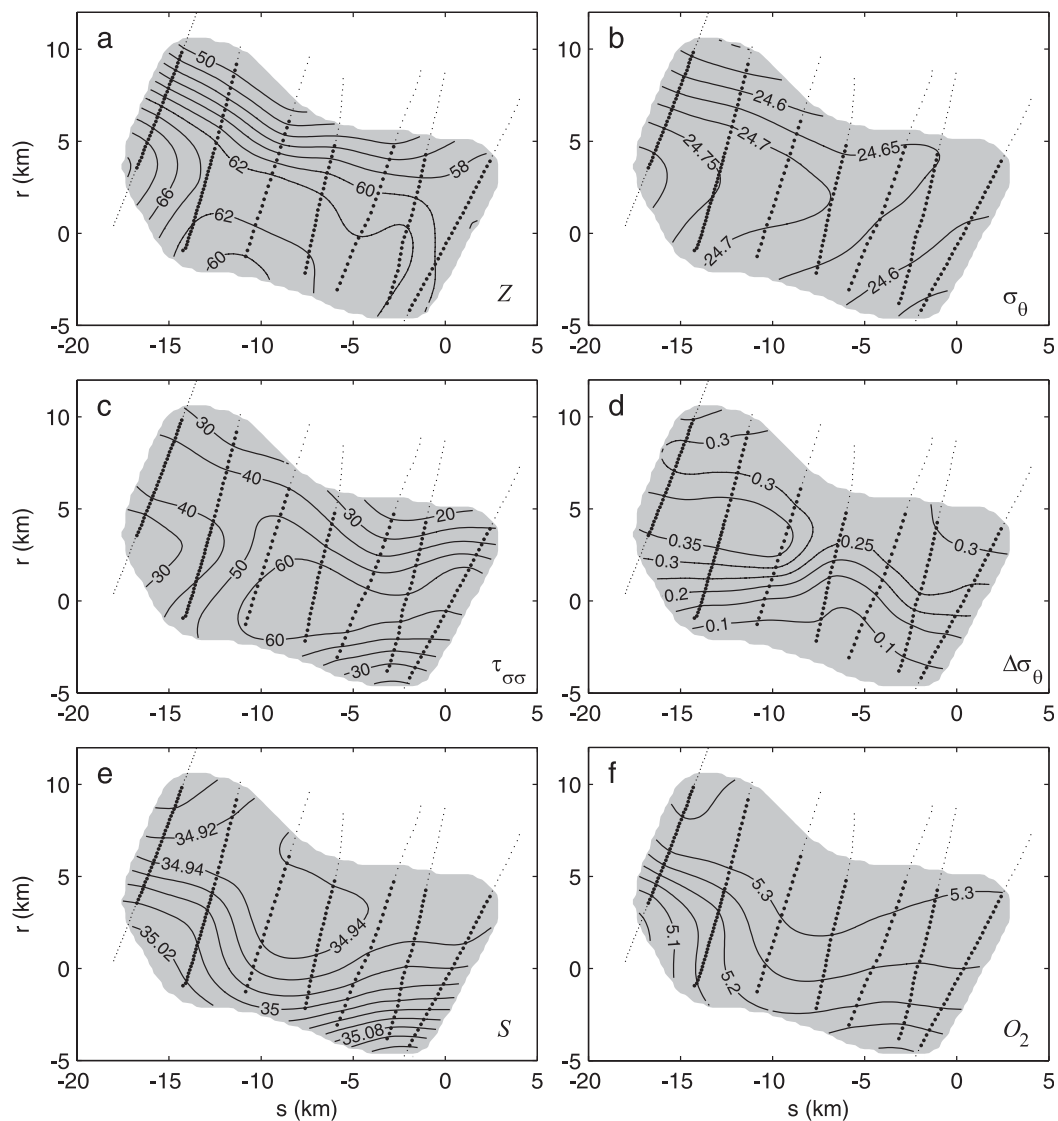


FIG. 10. Lateral distribution of the core parameters of a prominent intrusion in segment Bravo, based on a quasi-synoptic SWIMS survey on 14 Jul (deployment 12): (a) actual depth (m), (b) potential density (kg m^{-3}), (c) diapycnal spiciness curvature ($\text{m}^3 \text{kg}^{-1}$), (d) diapycnal intrusion thickness (kg m^{-3}), (e) salinity (practical salinity scale, nondimensional), and (f) dissolved oxygen concentration (mL L^{-1}). Intrusion core was defined as the local $\tau_{\sigma\sigma}$ maximum exceeding $10 \text{ m}^3 \text{ kg}^{-1}$; approximate lateral extent of the core is shown by gray shading. Location of individual SWIMS profiles are marked with light and dark dots, depending on whether the intrusion core was detected in a particular profile or not.

the vicinity of a particular intrusion. This float recorded a Lagrangian time series of salinity, temperature, and pressure at 30-s intervals, while closely following the motion of the surrounding seawater (D'Asaro 2003). SWIMS and MMP profiles taken within 500 m of the float illustrate the evolution of vertical structure in areas Bravo, Charlie, and Delta within the frontal zone (Fig. 12). Float deployment Alpha spanned only 24 h and is not shown. It should be kept in mind that float-referenced observations are “Lagrangian” only with respect to the

layer in the immediate vicinity of the float. Note also that using the semi-Lagrangian depth as a vertical coordinate removes the effects of isopycnal heaving and vertical strain; remaining variability can be attributed to sheared isopycnal advection and, possibly, mixing.

The largest intrusions likely persisted longer than they were tracked: for example, the Bravo intrusion was observed, at least partially, between 13 and 20 July. Consequently, the lifespan of these features is on the order of days, perhaps even weeks.

TABLE 1. Gradients of the depth and density of the “broad sheet intrusion” core (\pm standard error of the fit).

	Cross-front gradient ($\partial/\partial r$)		Alongfront gradient ($\partial/\partial s$)
	$R < 2 \text{ km}$	$R > 2 \text{ km}$	
$\nabla z (\times 10^{-3})$	-0.16 ± 0.14	-2.2 ± 0.14	-0.14 ± 0.05
$\nabla \sigma_\theta (\times 10^{-5} \text{ kg m}^{-4})$	1.61 ± 0.08	-3.6 ± 0.16	-0.92 ± 0.03

The structure of the intrusions did change during the tracking period owing to differential advection. Isopycnal variability in the vertical profiles was relatively weak during the Bravo float deployment (Figs. 12a,b), becoming much more pronounced during the Charlie and Delta deployments (Figs. 12c–f). Partially, this may be due to the weaker rms baroclinic velocities during the Bravo deployment (4 cm s^{-1}) compared to 6 cm s^{-1} during subsequent segments. Smoother lateral salinity structure of the Bravo intrusion (cf. Figs. 5 and 8) may also have been a factor.

Deviation of hourly salinity profiles from the mean showed signs of variability on time scales close to the inertial period $T_{\text{in}} = 2\pi f^{-1} = 23.2 \text{ h}$. Inertial variability of the salinity profiles was particularly pronounced during the Charlie segment (Fig. 13). This variability was largest at $\sigma_\theta \approx 24.6$, and 25.1 kg m^{-3} ($z_{\text{SL}} \approx 59$ and 100 m , respectively), while salinity at the float ($\sigma_\theta = 24.9 \text{ kg m}^{-3}$, $z_{\text{SL}} = 85 \text{ m}$) remained relatively constant as the float tracked its surrounding water. Temporal salinity variations above and below the float were negatively correlated (correlation coefficient -0.34 , significant at 60% with approximately eight degrees of freedom). The diapycnal wavelength of these oscillations was $O(0.8 \text{ kg m}^{-3})$, corresponding to about 80 m in the vertical.

3. Mesoscale background of submesoscale intrusions

Thermohaline gradients in the STFZ are constantly advected and distorted by mesoscale turbulence. Meandering filament structures are evident in the sea surface temperature satellite imagery (Fig. 1). The presence of the coherent intrusions in the STFZ may be intrinsically connected to the structure of the mesoscale advection field.

a. Structure of the mesoscale meander

During 7–26 July 2007, the survey focused on the outer edge of a mesoscale feature, identifiable as a relatively warm filament in sea surface temperature imagery (Fig. 1a). Within the filament concentration of intrusions near the two thermohaline fronts (referred to as F1 and F2) suggests that these were the regions of formation for interleaving features.

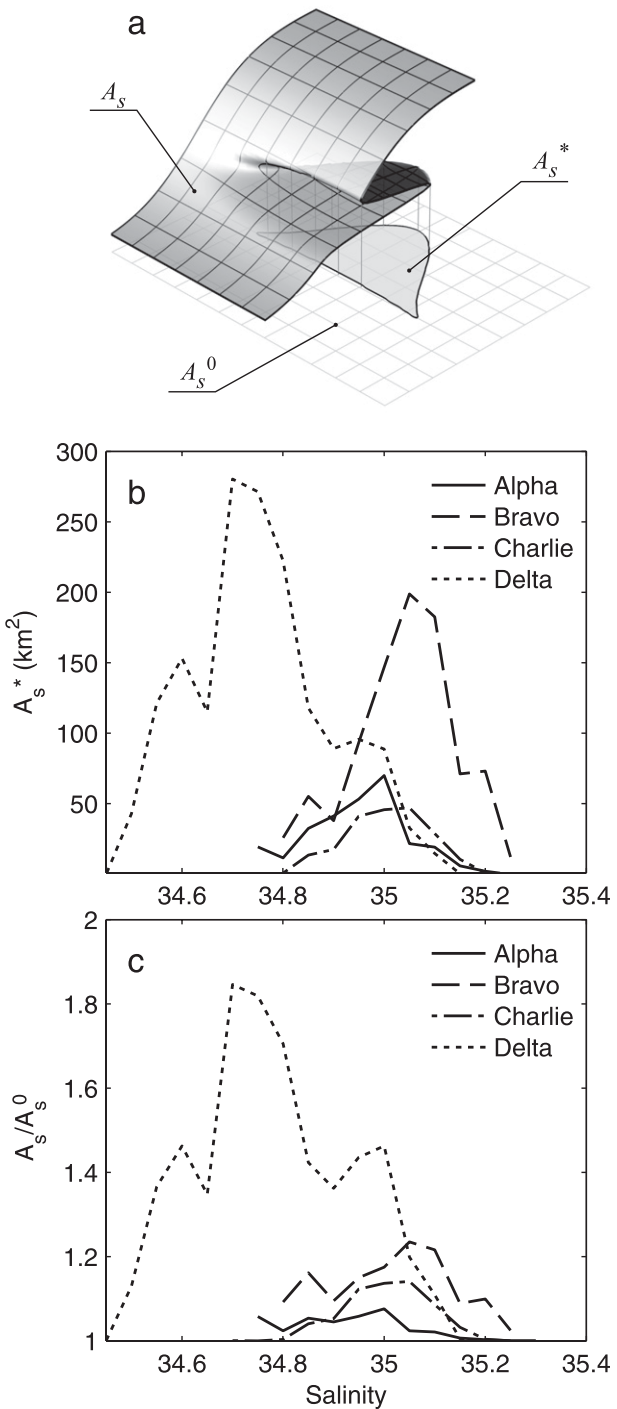


FIG. 11. (a) Schematics for an example calculation of area of deformation, A_s^* , of an arbitrary isohaline surface (a part of the surface removed for clarity, see text for details). (b) Area of deformation, A_s^* , and (c) deformation ratio, A_s^*/A_0 , of isohalines in four survey segments based on SWIMS surveys on 8 Jul (Alpha, solid line), 14 Jul (Bravo, dashed line), 20 Jul (Charlie, dash-dot line), and 23 Jul (Delta, dotted line). The shapes of representative isohaline surfaces for each survey are shown in Figs. 4–8.

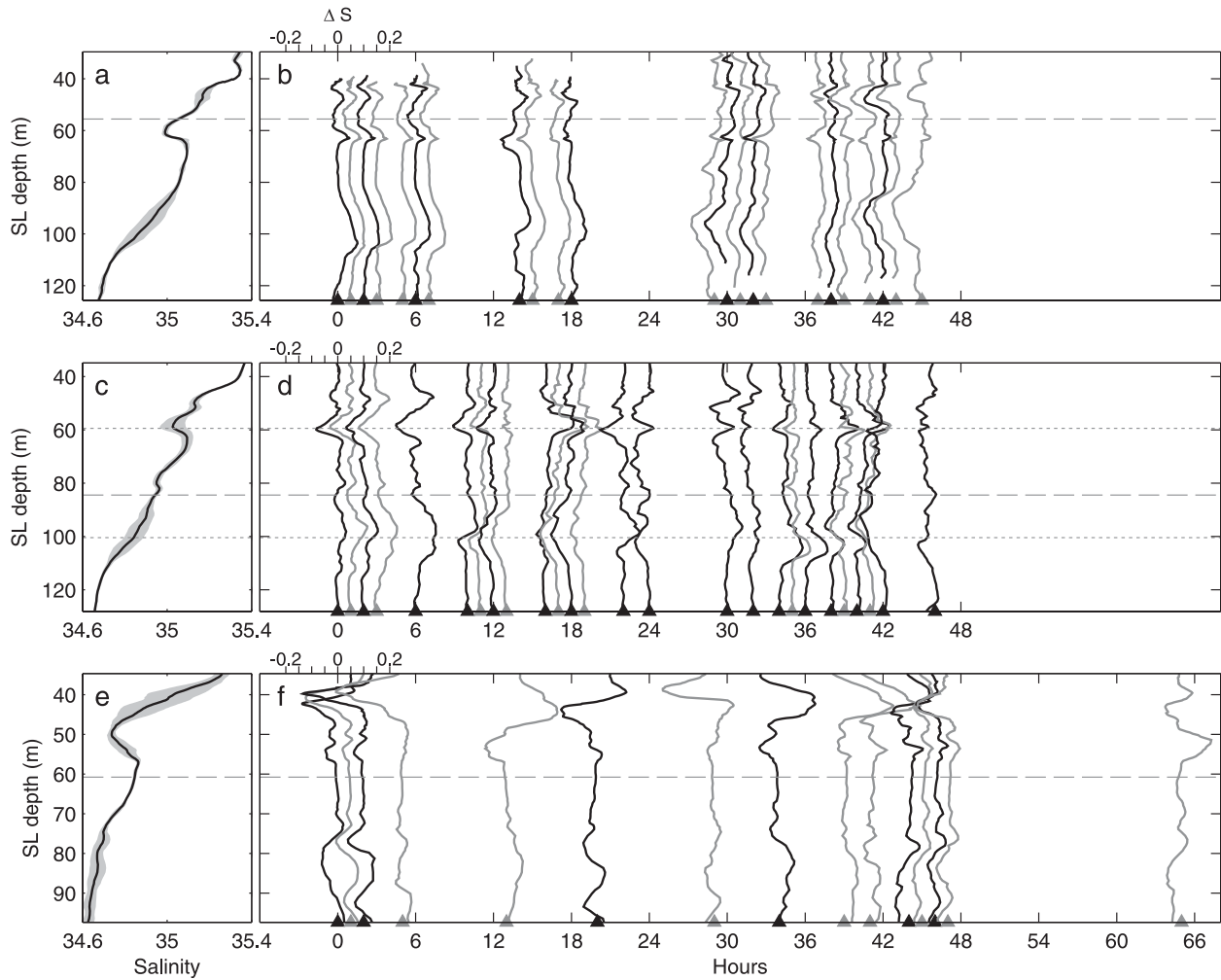


FIG. 12. (left) Mean vertical salinity profiles and (right) the deviations of hourly averages from the mean during the (a),(b) Bravo, (c),(d) Charlie, and (e),(f) Delta segments. Mean and deviation profiles are based on SWIMS and MMP data taken within a 500-m vicinity of the Lagrangian float; shading, alternating every hour, is used for clarity; timing marked by triangles. The salinity anomaly scale shown in the top left corner is correct for the first profile; subsequent profiles are offset by 0.05 h^{-1} . Horizontal dashed lines show the mean SL depth of the float deployment. Levels of strongest variability discussed in text are marked by horizontal dotted lines in (c),(d).

Average radial structure across this arc of the meander is shown in Fig. 14. Salinity (Fig. 14a) and temperature (not shown) decrease with depth and radius, forming two distinct fronts: F1 near $r = 158 \text{ km}$ and F2 near $r = 195 \text{ km}$. The fronts are partially compensated and barely noticeable in the density structure (Fig. 14b).

Throughout the STFZ, salinity decreases with depth, making most of the water column mildly susceptible to double-diffusive salt-fingering instability. The relative importance of the double-diffusive effects is expected to be related to the vertical density ratio, $R_\rho = (\alpha\theta_z)/(\beta S_z)$, where θ is the potential density, S is the salinity, and $\alpha = -\rho^{-1}(\partial\sigma/\partial\theta)_{S,p}$ and $\beta = \rho^{-1}(\partial\sigma/\partial S)_{\theta,p}$ are the coefficients of thermal expansion and saline contraction, respectively (St. Laurent and Schmitt 1999). Mean hydrographic structure observed during the experiment

typically has R_ρ between 3 and 5, with a median of 3.9. Such high density ratios ($R_\rho > 2$) suggest weak susceptibility to salt-fingering instability, while not excluding it completely.

The tangential velocity V_s is overwhelmingly clockwise (positive), forming two narrow surface-intensified jets near $r = 162$ and 189 km with the speeds reaching 0.4 m s^{-1} (Fig. 14d, Fig. 15a). Based on the deeper-reaching 75-kHz ADCP observations (not shown), V_s decreased exponentially below the core with an e -folding scale $\sim 180 \text{ m}$, reaching 0.11 m s^{-1} at 250 m depth. Below that, the decay in velocity weakens, with an e -folding scale of 650 m . Tangential advection is very small ($< 0.06 \text{ m s}^{-1}$) at 600-m depth. Anticyclonic tangential advection was largely in thermal-wind balance with the density field (Fig. 16). Relative vorticity $\zeta = -dV_s/dr - r^{-1}V_s$

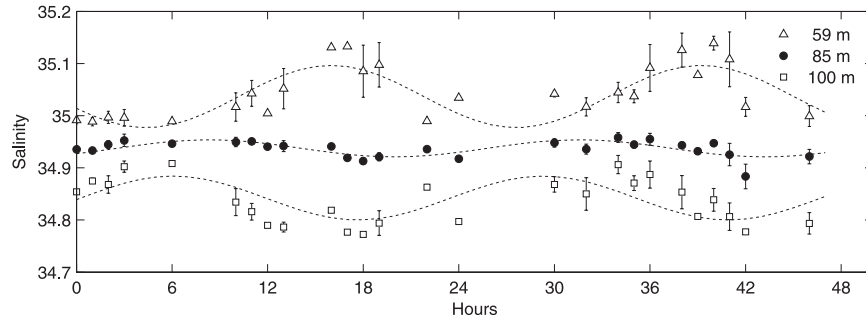


FIG. 13. Hourly averages of salinity at three SL levels based on SWIMS and MMP data taken within a 500-m vicinity of the Lagrangian float during deployment Charlie. The levels of maximal salinity variability (59 and 100 m, open symbols) were selected, along with the middle level (85 m, solid circles) corresponding to the mean SL depth of the float (levels marked in Fig. 12c). Error bars indicate one standard deviation of salinity for each hourly interval. Least squares fit of sinusoids with the inertial period $T_{\text{in}} = 2\pi f^{-1} = 23.2$ h to each of the time series are shown with dotted lines. Note that we do not imply that variability is necessarily inertial, as the time series are too short for harmonic analysis.

associated with the radial shear within the two jets over $O(10$ km) horizontal scales reached $-0.2f$ and $+0.4f$ (Fig. 15c). Large-scale vorticity associated with the meander itself, $\zeta_0 = -r^{-1}V_s$, was $O(-0.01)f$.

Even though tangential flow dominated the circulation, the relatively weak radial advection drives the cross-frontal growth of the intrusions. Radial velocity V_r was nearly zero within the jet cores, increasing slightly toward both the smaller and larger radii (Figs. 14d and 15b). Assuming two-dimensional dynamics, radial variation of V_r suggests the presence of bands of convergence ($r \approx 155$ and 175 km) and divergence ($r \approx 170$ and 190 km), with the strain rate $\chi = r^{-1}d(rV_r)/dr$ exceeding $\pm 0.1f$ (Fig. 15d).

Strong radial variability of V_s indicates that the eddy was not in solid-body rotation (Fig. 15a). In fact, the velocity distribution is closer to that of a nested pair of the so-called circular pulsions, analytical approximations developed for inertially oscillating warm-core frontal eddies with radially symmetric parabolic isopycnals (Rubino et al. 1998).

Substantial deformation of the thermohaline features due to differential tangential advection can be expected. A tangential velocity difference of 0.15 m s^{-1} between the initially radially aligned water parcels at $r = 160$ km and $r = 170$ km would result in their separation at a rate of 13 km per day. Over the 6-day survey period this separation would reach $O(80)$ km. A similar V_s difference of 0.15 m s^{-1} across the top 100 m (Fig. 14e) would result in similar rate of separation of parcels initially aligned vertically. These estimates illustrate that the evolution of the intrusions is necessarily affected by the structure of mesoscale [$O(100)$ km] advection, governed by geostrophic turbulence within the STFZ.

The fields of mean and rms vertical shear (Figs. 14e,f) were dominated by radial velocities, which were considerably more variable than tangential ones (cf. Figs. 14c,d). As expected, strongest shear variability occurred at the base of the mixed layer at $40\text{--}50$ -m depth. There was no apparent association of high shear with the localization of the intrusions. Furthermore, no particular enhancement of shear variance in the vicinity of F1 and F2 fronts consistent with near-inertial wave trapping (Kunze and Sanford 1984) was observed, possibly due to these fronts being narrower than the lateral coherence scale of the waves.

b. Effect of cross-front differential advection

The relationship between the hydrographic and velocity fields surveyed concurrently during the experiment can be investigated by prognostic simulation of cross-frontal tracer advection. The evolution of the hydrographic structure advected by cross-front ADCP velocities is used here to test whether the observed thermohaline intrusions could have been created by the observed velocity fields.

In a simple prognostic simulation, an initial salinity distribution on a cross-frontal section is advected by a velocity field, varying in a prescribed manner in time and space. Because the full three- and four-dimensional fields of salinity and velocity distribution are not available, two simplifying assumptions need to be made. First, the intrusions are considered to be purely two-dimensional, having infinite alongfront extent. With this assumption, alongfront gradients are neglected and the evolution of the intrusions is driven solely by cross-front velocities. Sheetlike intrusions, such as the intrusion Bravo, naturally lend themselves to such simplification.

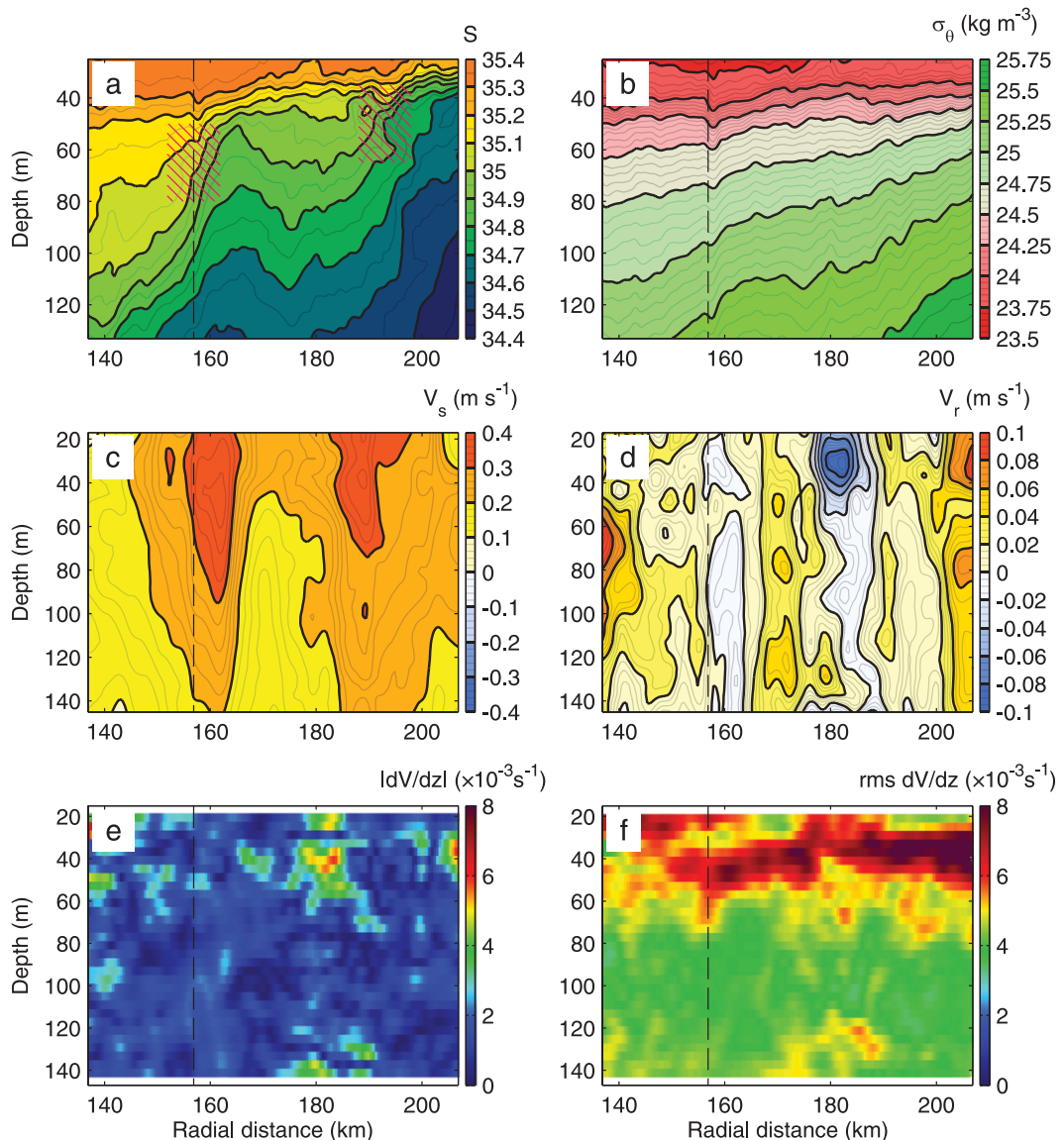


FIG. 14. The mean radial structure of the meander branch, based on shipboard ADCP and SWIMS observations 12–21 Jul 2007: (a) salinity, (b) potential density, (c) tangential velocity, V_s (positive clockwise), (d) radial velocity, V_r (positive outwards), (e) mean absolute vertical shear, and (f) rms vertical shear. Red hatching in (a) indicates the areas where the most prominent intrusions were observed. Vertical dashed line marks the reference radius $R_0 = 157$ km.

Second, the velocity field is assumed laterally homogeneous, varying only with time and depth. With this assumption, we can extrapolate the velocity profile measured by the shipboard ADCP onto the full extent of the cross-front section. This simplification is reasonable for radial velocity, which, unlike the tangential component, shows little coherent cross-front variability (see section 3a; Fig. 14d).

Using these assumptions, we simulate the evolution of frontal zone stratification in the Lagrangian segment Bravo between 13 and 20 July 2007. The initial salinity distribution was taken from the cross-frontal section

near ARF $s = 14$ km occupied during the SWIMS deployment 11 on 13 July (Fig. 17a). Insignificant salinity inversions present in this section were eliminated from initial conditions by low-pass filtering and sorting in the vertical (Fig. 17d). Cross-frontal advection was then simulated by time integration of the radial velocities, which produced relative shifting of various layers of the section. Barotropic advection, moving the section radially without distorting its structure, was neglected.

After four days of advection (corresponding to 17 July), a prominent low-salinity intrusion was formed at about 45 m SL depth (Figs. 17b,e). The structure of

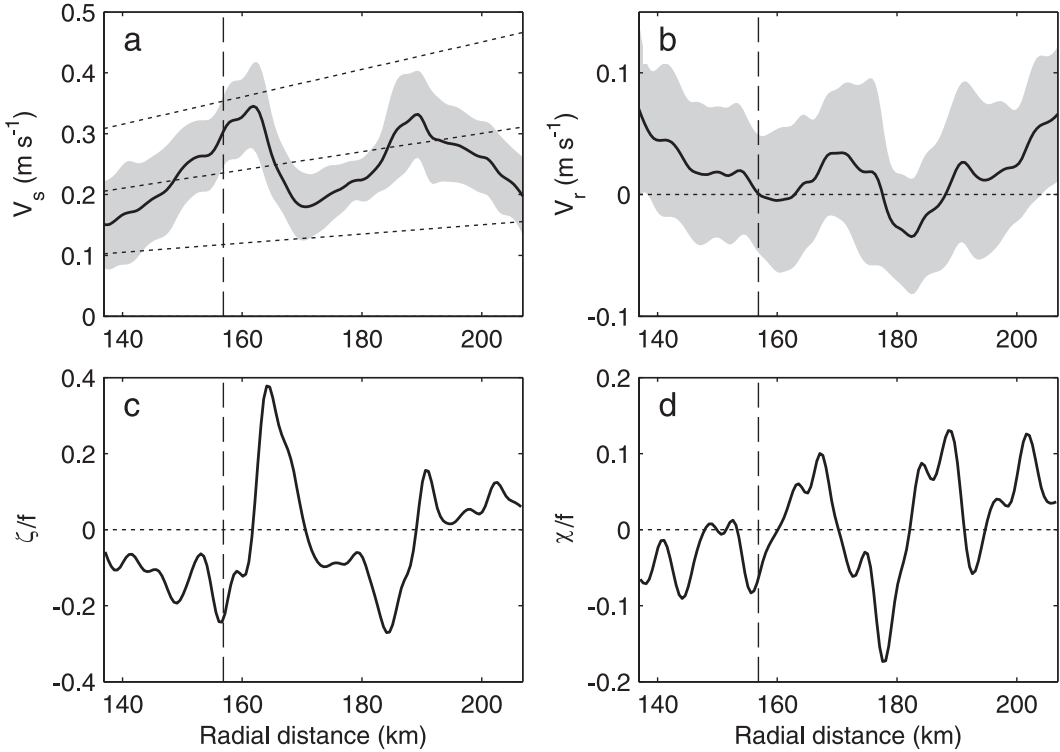


FIG. 15. The mean radial structure of the meander branch, based on shipboard ADCP observations 12–21 Jul 2007, averaged over the top 50 m: (a) tangential and (b) radial velocities, (c) relative vorticity, $\zeta = -dV_s/dr - r^{-1}V_s$, and (d) strain rate, $\chi = r^{-1}d(rV_r)/dr$. Gray shading indicates one standard deviation; dotted lines in (a) show radial dependence of the velocities assuming solid body rotation at rates of 1, 2, and $3 \times 10^{-2} f$. Vertical dashed line marks the reference radius $R_0 = 157$ km. Vorticity and divergence are calculated under the assumption of tangential invariance.

this intrusion is qualitatively similar to that of intrusion Bravo observed during the SWIMS deployment 15 on the same date at $s = 7$ km (Figs. 17c,f). At that time, the simulated differential shift between the 45- and 60-m layers reached 3.7 km (Fig. 18), similar to the extent of isohaline retroflection observed during the deployment 15 (4–5 km). It is interesting to note that the maximum differential displacement relative to the 50–60-m layer (>10 km) was reached near 33-m depth (Fig. 17b), yet the strongest low-salinity “intrusion” (as seen by the distortion of isopycnals) appeared at least 10 m deeper. Apparent absence of the intrusion in the upper layers is a result of weaker cross-front salinity gradients found in the mixed layer. This illustrates the critical and non-trivial dependence of the vertical structure of an intrusion on the vertical shear and on both lateral and vertical tracer gradients. Thus simple inference of an advection history based solely on the appearance of the intrusive features may be misleading (SGAH09).

The growth history of cumulative differential radial advection between the intruding layer and the underlying water (Fig. 18) suggests that both inertial and low-frequency processes contribute to the evolution of

intrusions. Inertial oscillations cause relative displacement of the layers with amplitudes up to 2 km. The time scale of subinertial advection was probably longer than 20 days, though not adequately resolved with these observations. The maximum rate of low-frequency differential advection was $O(10^{-2} \text{ m s}^{-1})$, or 1 km day^{-1} . The vertical structure of inertial and subinertial advection, determined by an empirical orthogonal function analysis (not shown), was similar—both showing a reversal in the flow near 45 and 80 m.

We do not imply that our kinematic simulation realistically predicts the formation of the intrusion Bravo during 13–17 July 2007. In fact, this intrusion had probably existed prior to 13 July, albeit slightly farther upstream (see section 2a; Fig. 5). The simulation results, however, do show that the structure of the observed velocity field was favorable to the formation of intrusions of realistic scales. Note that Fig. 17b also illustrates the important observation (Woods et al. 1986) that purely isopycnal lateral advection is capable of creating features slanted across isopycnals. Consequently, no process leading to Lagrangian density change necessarily needs to be invoked to explain such slopes that may be observed.

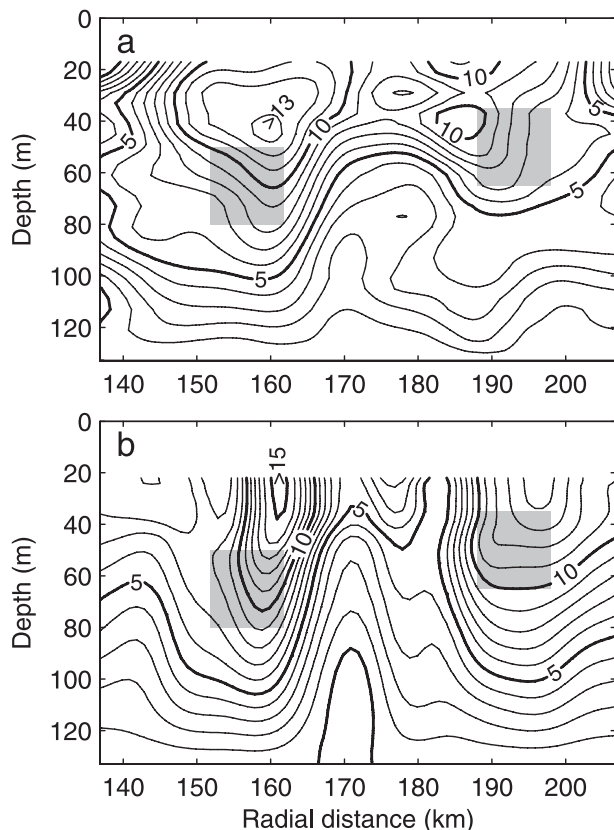


FIG. 16. Distribution of (a) observed and (b) geostrophic tangential velocity on a radial section (10^{-2} m s^{-1}). Geostrophic calculations are based on the mean radial density distribution observed during the 12–21 Jul 2007 SWIMS surveys (Fig. 14b). Observed velocities are based on the average of shipboard ADCP data 12–26 Jul 2007 (Fig. 14c). Both estimates are referenced to 130-m depth and smoothed horizontally with a 10-km wide low-pass filter. Gray shading indicates where the most prominent intrusions were observed.

4. Summary and discussion

a. Summary

Frontal intrusions were followed and their evolution mapped in three dimensions. At least two substantially different types of intrusions were observed: sheets and tongues. The sheets were $O(10 \text{ m})$ thick, protruding about 10 km into the warm, saline side of the front, and were coherent for 10–30 km along the front. Having about the same thickness and cross-frontal extent as the sheets, tongues extended less than 5 km along the front. Two tongues were found together. All the intrusions were attached to the front; no isolated lenslike structures were observed. Intrusions originated from the isohalines of 34.8 to 35.0, appearing most often at the steepest part of the front. On the other hand, these isohalines were devoid of

intrusions for at least a 50-km stretch elsewhere along the front.

All of the intrusions persisted as long as we followed them, several days to one week. Because they evolved so slowly, neither their formation nor decay were documented. Prognostic kinematic simulation of deformation of the cross-front hydrographic structure by the observed advection (section 3b) produced features similar in scale, location, and shape to the observed sheetlike intrusions. This suggests that they could have been produced by distortion of the thermohaline field by observed velocities. Consequently, the dynamic formation of these intrusions is at least partially observable, in contrast to the flows driven by double-diffusive instabilities that are too weak for ADCP field observation. The evolution of the intrusions appears to occur on inertial [$O(24 \text{ h})$], and subinertial [$O(10 \text{ days})$] time scales.

b. Observational technique

Single three-dimensional maps of intrusions extending over submesoscale distances (several tens of kilometers) can be made over the course of several hours, once the local orientation of the front is determined from SST imagery or a large-scale survey. It is possible to construct a sequence of such maps by tagging and tracking the feature of interest with a physical, or with a “virtual” float if the mesoscale flow is predictable. Strong and persistent vertical and lateral shears over scales comparable to those of the intrusion make Lagrangian tracking of a particular water parcel irrelevant over prolonged periods of time. The synoptic differential advection of water parcels in an intrusion was approximately 10 km day^{-1} . Depending on lateral thermohaline gradients, this advection may enhance, eliminate, or displace the intrusion as a whole, or it may leave it unchanged.

The single-ship surveying mode had limited capacity to resolve variability of intrusions on the smaller [$O(1 \text{ km})$] and larger [$O(10 \text{ km})$] scales simultaneously. The need to alternate small- and large-scale survey patterns inevitably resulted in loss of spatial and temporal resolution, making the structure of the features ambiguous and reducing confidence in tracking.

c. Implications for lateral mixing

Coherent intrusions observed in STFZ are associated with cross-front transport of temperature and salinity and, therefore, are directly related to lateral mixing of tracers. It is presently not clear how this mixing can be parameterized.

Typical methods of estimation of lateral fluxes due to fine structure are based on the balance of lateral advection and vertical diffusion (Joyce 1977) and are not applicable here. Diffusive time scale H^2/K of the large

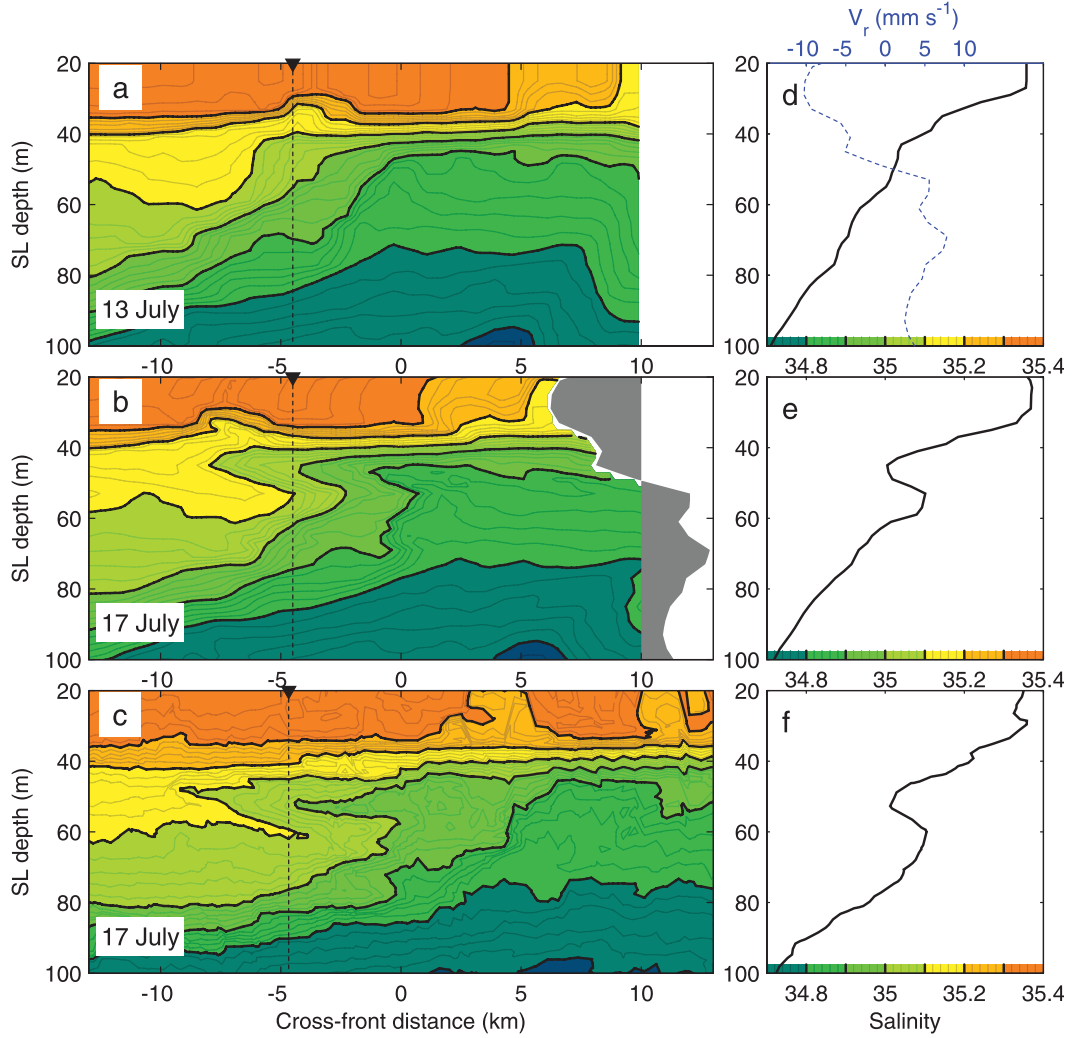


FIG. 17. Simulation of the effects of differential advection. (a) Hypothetical initial salinity distribution, based on SWIMS survey on 13 Jul (deployment 11). (b) Distorted salinity field after four days of realistic cross-front advection. (c) Cross-front salinity distribution observed during SWIMS survey on 17 Jul (deployment 15). (d)–(f) Salinity profiles at $r = -4.5$ km [location marked by vertical dashed lines in (a)–(c)]. Blue dashed line in (d) shows the mean radial velocity over the simulation period. Gray shading in (b) corresponds to distortion of an initially vertical profile.

intrusions observed in STFZ is $O(100$ days), assuming thickness $H = O(10\text{m})$ and typical vertical eddy diffusivity $K = O(10^{-5} \text{ m s}^{-2})$, which is substantially longer than the presumed lifespan of the intrusions (days to weeks; see section 2d). Therefore, steady-state balance theory cannot be applied here.

At the same time, the evolution of intrusions during STF07 was not rapid enough to allow gathering of reliable statistics of their realizations during the month-long single-ship experiment. Consequently, statistical estimation of effective tracer diffusivity due to STFZ intrusions was also not possible. Moreover, it is not clear whether the dispersion of tracers attributable to these features can be described in terms of a diffusive (i.e., downgradient flux)

model or whether a “transient” model (Stull and Kraus 1987) that includes parameterization of nonlocal eddy transport is necessary.

The question remains whether the observed intrusions and associated tracer fluxes are purely random or at least partially deterministic. The large singular features observed during the STFZ experiment suggested predominance of low-salinity tongues and sheets extending toward the warm and salty side of the front. Absence of large features of opposite sign may be indicative of the asymmetry of the interleaving dynamics, common among submesoscale ageostrophic processes (Capet et al. 2008b). On the other hand, it could be purely coincidental, considering a relatively small sample of the observed structures.

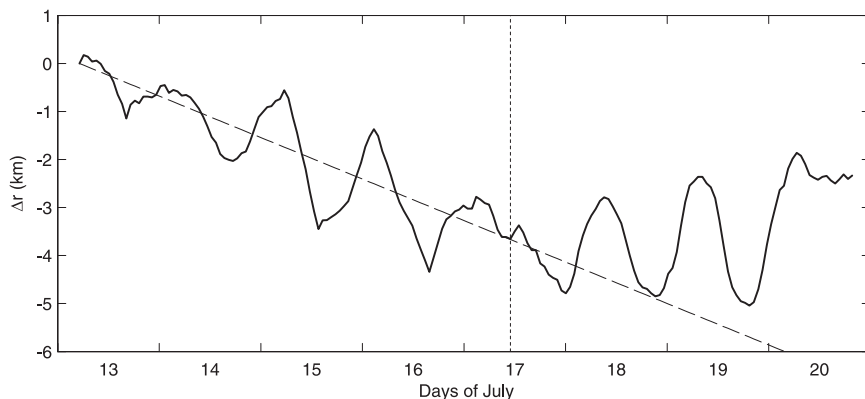


FIG. 18. Estimated radial displacement at 45-m depth relative to that at 60 m. The dashed line shows steady advection rate of -0.01 m s^{-1} ($\sim 1 \text{ km day}^{-1}$) for reference. Vertical dotted line marks the timing of the section in Fig. 17b.

d. Driving dynamics

Most intrusions observed in the STFZ do not have the characteristics of double-diffusive interleaving (SGAH09). An alternative explanation for the observed structures can be sought among the broad range of submesoscale frontal processes, known to create intricate lateral filamentation on scales of 1–10 km (Mahadevan and Tandon 2006). Among these processes is stirring by balanced geostrophic turbulence (McWilliams et al. 2001), spontaneous ageostrophic instabilities (Molemaker et al. 2005), nonlinear Ekman effects (Thomas and Lee 2005), and internal frictional effects (Garrett and Loder 1981). Since these processes tend to occur simultaneously (Capet et al. 2008a), conclusive differentiation between them requires detailed balance analysis through inverse modeling (e.g., Thomas et al. 2010) and is not feasible with the available data.

The process of intrusion formation in STFZ appears to be essentially similar to that of the submesoscale surface frontal cusps and filaments (A. Mahadevan, A. Tandon, and J.-L. Thiffeault 2010, unpublished manuscript), except that the resulting features have no surface expression due to the capping by the summertime mixed layer. Formation of thermohaline filaments of increasingly small vertical and horizontal scales is a common feature of mesoscale turbulent flows associated with the double cascade of density and spice variance (Klein et al. 1998; Smith and Ferrari 2009). Therefore, dynamics of the intrusions is inseparable from the dynamics of the mesoscale meandering of STFZ, which appears to be governed by well-balanced geostrophic turbulence (section 3a). This turbulence likely develops from the spontaneous instability of lateral density gradients within the winter mixed layer (Hosegood et al. 2006). Symmetric instability, which is a common source of mixed layer

submesoscale turbulence (Boccaletti et al. 2007), may play an important role during the initial stages of this development. During the summertime STF07 surveying, however, potential vorticity was typically positive in the restratified mixed layer between 30 and 100 m (not shown, but can be inferred from Figs. 14 and 15), indicating that symmetric instability was weak relative to the slower, more balanced baroclinic modes. Mesoscale frontogenesis that creates sharp thermohaline fronts, such as F1 and F2 in STFZ, may trigger partial loss of balance when the strain rate S exceeds absolute vorticity A (Molemaker et al. 2005). Even though the time-space aliasing did not allow robust estimation of the strain rate in STF07, this condition, $A-S < 0$, was apparently satisfied in several locations on the anticyclonic side of F1 and F2. Evidence of inertial variability in the structure of the STFZ intrusions (section 2d) supports the potentially important role for unbalanced dynamics.

Acknowledgments. We thank Paul Aguilar, Steve Bayer, Eric Boget, Andrew Cookson, Ryuichiro Inoue, Jack Miller, Avery Snyder, Dave Winkel, as well as the crew of R/V *Wecoma* for their invaluable help collecting the data. Jules Hummon of the University of Hawaii provided invaluable help setting up UHDAS on *Wecoma*. We also thank Amala Mahadevan and Amit Tandon for stimulating discussion and four anonymous reviewers for their helpful comments. This work was supported by the National Science Foundation under Grant OCE0549948.

APPENDIX A

Tracking and Forecast of Float Trajectory

The Lagrangian float was tracked acoustically using two independent systems: range-only tracking with the

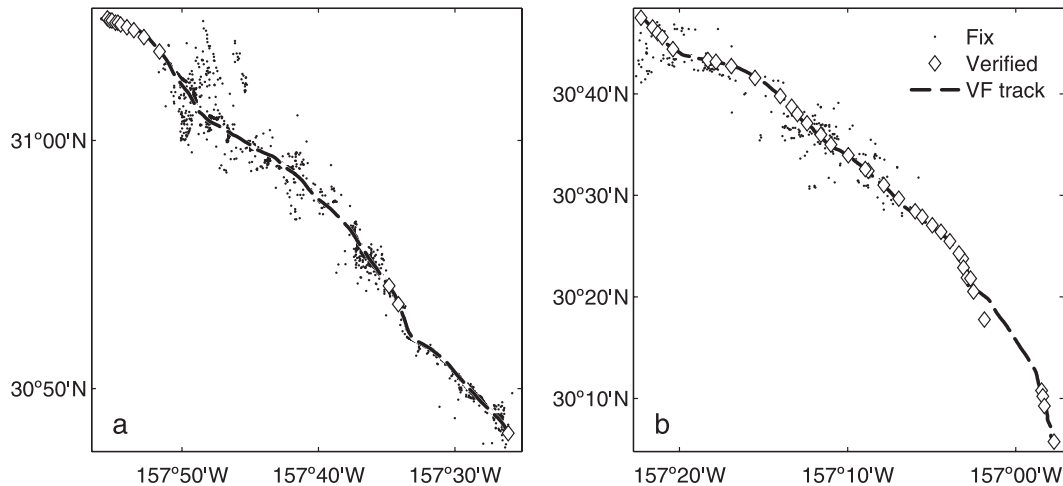


FIG. A1. Reanalysis of drift trajectory (dashed line) for two deployments of the float: (a) Bravo (14–16 Jul 2007) and (b) Charlie (18–21 Jul 2007). Dots mark the cloud of acoustic float position fixes. Manually verified fixes are marked by diamonds.

hull transducer and range-heading tracking with a directional TrackPoint II system on an over-the-side boom mount. The float acoustically transmitted measured density values encoded as a delay between two consecutive “pings.” In addition to confirming position of the float relative to the target isopycnal, decoded density values helped to identify corrupted range/heading packets, which tend to have density data corrupted as well. Even though this method could not eliminate all stray packets, it reduced rms scatter of float fixes by a factor of 2. While the TrackPoint provided superior float location, it could only be operated reliably at moderate ship speed (<3 kt).

The hull transducer could be operated at higher transit speed, but it provided only range to the float. Range-only tracking of a target is a challenging nonlinear estimation problem, which can theoretically be addressed with Kalman filtering (e.g., Cevher et al. 2006). In practice, intermittency and noisiness of range data resulted in poor convergence of this method. Estimating the float location visually from the intersection of automatically plotted range circles proved to be more robust.

The float trajectory was continuously estimated by time integration of shipboard ADCP velocity observations at the nominal depth of the float. The high lateral coherence of the velocity field was sufficient to allow inference of the float advection despite the large separation at times between the float and the vessel. The “virtual float” (VF) trajectory (Fig. A1) was then adjusted to fit all available position fixes in the least squares sense, taking into account differences in their reliability (e.g., GPS positions of the float deployment

and recovery were considered more reliable than manual range-only tracking fixes).

This trajectory reanalysis was run concurrently with the SWIMS survey, providing predictions of the VF trajectory for the proximal several hours. This allowed extending the survey pattern beyond the range of acoustic contact with the float since the trajectory prediction could be used to direct the search for the float.

APPENDIX B

Advecting Reference Frame

Given the observed advection field (Fig. 3), a natural starting point for defining a working frame of reference is a cylindrical coordinate system $[\varphi, r, z]$, where φ is the azimuth (positive clockwise), r is the distance from the center of the arc, and z is the vertical coordinate. Such a coordinate system automatically takes into account the changes of the front orientation, which would be difficult to represent in rectangular coordinates.

Due to the presence of lateral and vertical shears, the choice of a reference trajectory for a frame of reference is not unique. Isopycnal float trajectories provide a natural reference except that 1) the float was deployed for only 8 of 14 days and 2) each float deployment was at a different density with no attempt to align it in any Lagrangian sense. Consequently, the “virtual float” approach (see appendix A) was extended to provide a self-consistent estimate of the advection for the duration of the survey. The reference trajectory was obtained by time integration of vertically averaged velocities

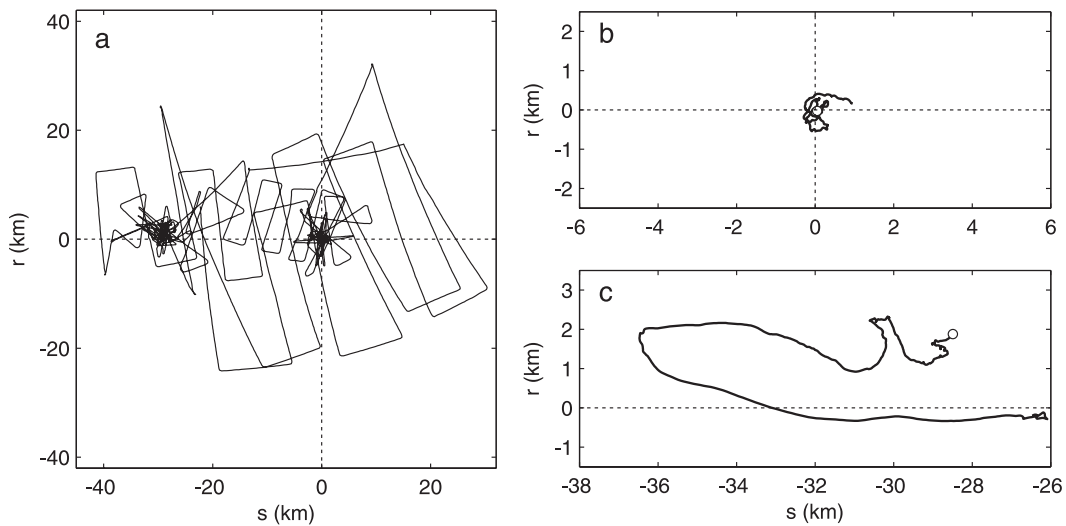


FIG. B1. (a) SWIMS survey track between 13 and 21 Jul (segments Bravo and Charlie, deployments 11–20) and float trajectories during the (b) Bravo and (c) Charlie deployments in advected reference frame. Float deployment locations are marked with circles in (b) and (c).

observed by shipboard ADCP between 50 and 65 m. Integration was done in polar coordinates. The depth interval and the constant of integration were chosen to provide best agreement with the VF trajectory during the first float deployment. Unlike the VF method, no actual float position information was assimilated into the reference trajectory estimate. This was done deliberately to allow uniform treatment of times with and without float data and to facilitate comparison with the VF trajectories.

The ARF coordinates are then given by the difference between a point's polar coordinates $[\varphi, r]$ and the reference trajectory $[\varphi_0(t), r_0(t)]$ at a given time t . So that both ARF coordinates are expressed in kilometers, the angular azimuthal distance $\varphi - \varphi_0(t)$ is expressed as circumferential distance $s = R_0[\varphi - \varphi_0(t)]$, where the mean radial distance of the first float deployment $R_0 = 157$ km is taken as the reference radius. It should be stressed, however, that the ARF coordinate system defined in this way is orthogonal, but not Cartesian.

Velocity measurements were projected onto the ARF axes to obtain tangential and radial components V_s and V_r , respectively. No scaling of the velocity components or subtraction of the VF advection was performed, unless specified explicitly. Thus the tangential advection of a particle in ARF, Δs , generally should not be assumed to be equal to the time integral of its tangential velocity V_s .

The SWIMS survey path and the float trajectories in the ARF are shown in Figs. B1 and B2. During the float deployment Bravo (14–16 July, Fig. B1b), the float excursions from the center of the ARF were on the order

of 0.5 km. The float deployment Charlie (18–21 July, Fig. B1c) was approximately 30 km upstream of Bravo (in the ARF), and also at a deeper level. The location of the float deployment Delta (Fig. B2b) was 98 km farther upstream and also 76 km toward the outer edge of the meander. Much greater ARF extent of the float trajectory during the latter two deployments (over 10 km) is another manifestation of layered differential advection.

While well-aligned with the mesoscale meander flow, ARF may have been occasionally misaligned with the local orientation of the salinity fronts. Continuous robust estimation of the location and orientation of the fronts was not feasible due to the complex shape of the isohaline surfaces (see section 2a). Consequently, a well-defined mesoscale ARF was preferred.

APPENDIX C

Thin-Plate Spline Smoothing

Objective mapping (OM, also known as optimal interpolation or objective analysis) is one method to interpolate the results of grid hydrographic surveys (e.g., Rudnick and Luyten 1996). OM requires a priori selection of the analytical approximation of the shape of covariance functions (Rudnick and Luyten 1996), which is particularly problematic in frontal zones where the property gradients are strong, anisotropic, and spatially nonstationary. Here, an alternative method using thin-plate smoothing splines (TPSS) was used. The main advantage of TPSS interpolation over OM is the automatic adaptation of the spectral characteristics of the

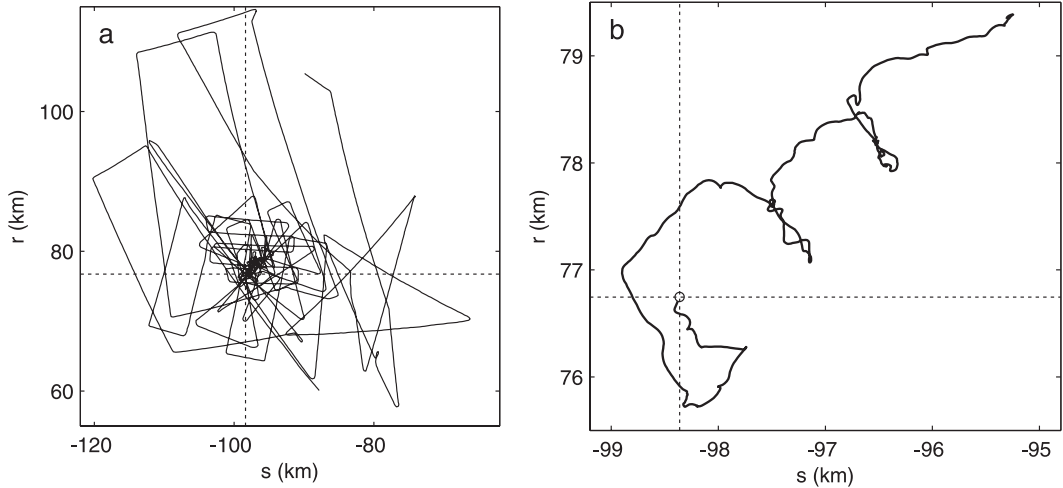


FIG. B2. (a) SWIMS survey track between 21 and 26 Jul (segment Delta, deployments 21–26) and (b) float trajectory during the Delta deployment in advected reference frame. Float deployment location is marked with a circle.

spatial filter to the specific data distribution. Unlike OM, TPSS provides sensible interpolation in data-void regions without oversmoothing densely sampled areas. See Sokolov and Rintoul (1999) for further discussion of the differences of interpolation methods.

TPSS approximation of scattered data $z_i = z(\mathbf{x}_i)$, where $\mathbf{x}_i = (x_i, y_i)$ are the data location coordinates, seeks the solution $\hat{z}(\mathbf{x})$ in the form

$$\hat{z}(\mathbf{x}) = \sum_{i=1}^n a_i \Psi(\|\mathbf{x} - \mathbf{x}_i\|), \quad (\text{C1})$$

where a_i are the weighting coefficients, and $\Psi(r) = r^2 \log r$ is a radial basis function (Wahba and Wendelberger 1980; Sokolov and Rintoul 1999). The coefficients a_i are chosen to produce the smoothest interpolant consistent with the data; mathematically, they minimize the energy function

$$J = \sum_{i=1}^n (z_i - \hat{z}(\mathbf{x}_i))^2 + \lambda \iint \left[\left(\frac{\partial^2 \hat{z}}{\partial x^2} \right)^2 + 2 \left(\frac{\partial^2 \hat{z}}{\partial x \partial y} \right)^2 + \left(\frac{\partial^2 \hat{z}}{\partial y^2} \right)^2 \right] dx dy, \quad (\text{C2})$$

where λ is a regularization parameter controlling the desired degree of smoothness of the interpolated field. Low smoothing parameter values ($\lambda \rightarrow 0$) produce an interpolating spline, while high ($\lambda \rightarrow \infty$) result in a least squares plane fit to the data (Fig. C1). A choice of the parameter between these two extreme cases can be either ad hoc or employ generalized cross-validation (Wahba and Wendelberger 1980) or L-curve (Hansen 1998) methods. A value of $\lambda = O(10)$ produced adequate mapping of SWIMS data.

APPENDIX D

Ambiguity of Three-Dimensional Mapping

Our procedure of three-dimensional mapping produces a gap in the feature between the two survey tracks between $s = 1$ and 5 km (Fig. 5). The tongue at $s = 5$ km, however, appears to be a natural extension of the upstream sloping feature. Isolation of thin sloping features into a series of “islands” arises from the fundamental

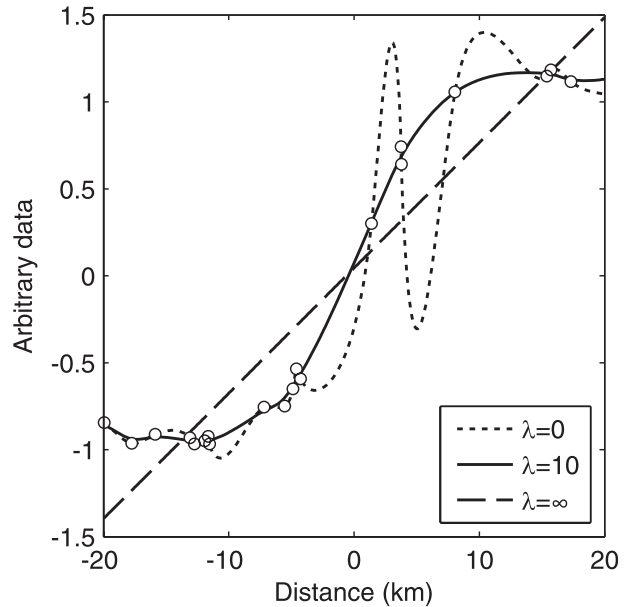


FIG. C1. Mapping of arbitrary scattered data (dots) using thin plate smoothing spline with different regularization parameters λ .

problem of spatial aliasing, inherent in relatively sparse sampling of a field containing high horizontal wave-numbers (Smith and O'Connell 2005). This problem could be mitigated if the slope of the feature could be determined a priori, an impossible task in our case—because the slopes vary not only from feature to feature but over the extent of individual intrusions as well. A variety of postprocessing algorithms that estimate local medium-scale gradients and iteratively apply anisotropic diffusion aligned with these gradients have been developed for antialiasing of computer imagery and geophysical data (e.g., Perona and Malik 1990; Smith and O'Connell 2005). Even though we successfully tested an anisotropic diffusion algorithm variation for individual sections, application to the full three-dimensional field is computationally expensive. More importantly, such postprocessing imposes some subjective constraints on the resulting map. These constraints could not be duly justified by the available data, so we choose not to apply postprocessing. It should be noted, however, that both the “connected” and “separated” interpretations are equally admissible given the available data.

REFERENCES

- Alford, M. H., M. C. Gregg, and E. A. Asaro, 2005: Mixing, 3D mapping, and Lagrangian evolution of a thermohaline intrusion. *J. Phys. Oceanogr.*, **35**, 1689–1711.
- Armi, L., D. Hebert, N. Oakey, J. F. Price, P. L. Richardson, H. T. Rossby, and B. Ruddick, 1989: Two years in the life of a Mediterranean salt lens. *J. Phys. Oceanogr.*, **19**, 354–370.
- Boccaletti, G., R. Ferrari, and B. Fox-Kemper, 2007: Mixed layer instabilities and restratification. *J. Phys. Oceanogr.*, **37**, 2228–2250.
- Capet, X., J. C. McWilliams, M. J. Molemaker, and A. F. Shchepetkin, 2008a: Mesoscale to submesoscale transition in the California Current system. Part II: Frontal processes. *J. Phys. Oceanogr.*, **38**, 44–64.
- , —, —, and —, 2008b: Mesoscale to submesoscale transition in the California Current system. Part I: Flow structure, eddy flux, and observational tests. *J. Phys. Oceanogr.*, **38**, 29–43.
- Cevher, V., R. Velmurugan, and J. H. McClellan, 2006: A range-only multiple target particle filter tracker. *Proc. IEEE Int. Conf. on Acoustics, Speech and Signal Processing*, doi:10.1109/ICASSP.2006.1661116.
- D'Asaro, E. A., 2003: Performance of autonomous Lagrangian floats. *J. Atmos. Oceanic Technol.*, **20**, 896–911.
- Fedorov, K. N., 1978: *The Thermohaline Finestructure of the Ocean*. Pergamon Press, 170 pp.
- Garrett, C. J. R., and J. W. Loder, 1981: Dynamical aspects of shallow sea fronts. *Philos. Trans. Roy. Soc. London*, **302**, 563–581.
- Gregg, M. C., 1980: The three-dimensional mapping of a small thermohaline intrusion. *J. Phys. Oceanogr.*, **10**, 1468–1492.
- , and C. S. Cox, 1972: The vertical microstructure of temperature and salinity. *Deep-Sea Res.*, **19**, 355–376.
- , and J. H. McKenzie, 1979: Thermohaline intrusions lie across isopycnals. *Nature*, **280**, 310–311.
- Hansen, P. C., 1998: *Rank-Deficient and Discrete Ill-Posed Problems: Numerical Aspects of Linear Inversion*. Society for Industrial and Applied Mathematics, 247 pp.
- Hitchcock, G. L., T. Rossby, J. L. Lillibridge, E. J. Lessard, E. R. Levine, D. N. Connors, K. Y. Børshøj, and M. Mork, 1994: Signatures of stirring and mixing near the Gulf Stream front. *J. Mar. Res.*, **52**, 797–836.
- Hosegood, P., M. C. Gregg, and M. H. Alford, 2006: Submesoscale lateral density structure in the oceanic surface mixed layer. *Geophys. Res. Lett.*, **33**, L22604, doi:10.1029/2006GL026797.
- Joyce, T. M., 1977: A note on the lateral mixing of water masses. *J. Phys. Oceanogr.*, **7**, 626–629.
- Klein, P., A. M. Treguier, and B. L. Hua, 1998: Three-dimensional stirring of thermohaline fronts. *J. Mar. Res.*, **56**, 589–612.
- Klymak, J. M., and M. C. Gregg, 2001: The three-dimensional nature of flow near a sill. *J. Geophys. Res.*, **106C**, 22 295–22 311.
- Kunze, E., and T. B. Sanford, 1984: Observations of near-inertial waves in a front. *J. Phys. Oceanogr.*, **14**, 566–581.
- Mahadevan, A., and A. Tandon, 2006: An analysis of mechanisms for submesoscale vertical motion at ocean fronts. *Ocean Modell.*, **14**, 241–256.
- , L. N. Thomas, and A. Tandon, 2008: Comment on “Eddy/Wind interactions stimulate extraordinary mid-ocean plankton blooms.” *Science*, **320**, 448b.
- McIntyre, M. E., 1970: Diffusive destabilization of the baroclinic circular vortex. *Geophys. Fluid Dyn.*, **1**, 19–57.
- McWilliams, J. C., M. J. Molemaker, and I. Yavneh, 2001: From stirring to mixing of momentum: Cascades from balanced flows to dissipation in the oceanic interior. *Proc. 'Aha Huliko'a Hawaiian Winter Workshop*, Honolulu, HI, University of Hawaii at Manoa, 59–66.
- Molemaker, M. J., J. C. McWilliams, and I. Yavneh, 2005: Baroclinic instability and loss of balance. *J. Phys. Oceanogr.*, **35**, 1505–1517.
- Perona, P., and J. Malik, 1990: Scale-space and edge detection using anisotropic diffusion. *IEEE Trans. Pattern Anal. Mach. Intel.*, **12**, 629–639.
- Roden, G. I., 1964: Shallow temperature inversions in the Pacific Ocean. *J. Geophys. Res.*, **69**, 2899–2914.
- Rubino, A., P. Brandt, and K. Hessner, 1998: Analytical solutions for circular eddies of the reduced-gravity, shallow-water equations. *J. Phys. Oceanogr.*, **28**, 999–1002.
- Ruddick, B., and O. Kerr, 2003: Oceanic thermohaline intrusions: Theory. *Prog. Oceanogr.*, **56**, 483–497.
- , and K. Richards, 2003: Oceanic thermohaline intrusions: Observations. *Prog. Oceanogr.*, **56**, 499–527.
- Rudnick, D. L., and J. R. Luyten, 1996: Intensive surveys of the Azores Front 1. Tracers and dynamics. *J. Geophys. Res.*, **101C**, 923–939.
- Schmitt, R. W., R. G. Lueck, and T. M. Joyce, 1986: Fine- and microstructure at the edge of a warm-core ring. *Deep-Sea Res.*, **33**, 1665–1689.
- Shcherbina, A. Y., M. C. Gregg, M. H. Alford, and R. R. Harcourt, 2009: Characterizing thermohaline intrusions in the North Pacific subtropical frontal zone. *J. Phys. Oceanogr.*, **39**, 2735–2756.
- Smith, K. S., and R. Ferrari, 2009: The production and dissipation of compensated thermohaline variance by mesoscale stirring. *J. Phys. Oceanogr.*, **39**, 2477–2501.
- Smith, R. S., and M. D. O'Connell, 2005: Interpolation and gridding of aliased geophysical data using constrained anisotropic diffusion to enhance trends. *Geophysics*, **70**, V121–V127.

- Sokolov, S., and S. R. Rintoul, 1999: Some remarks on interpolation of nonstationary oceanographic fields. *J. Atmos. Oceanic Technol.*, **16**, 1434–1449.
- Spilhaus, A. F., 1940: A detailed study of the surface layers of the ocean in the neighborhood of the Gulf Stream with the aid of rapid measuring hydrographic instruments. *J. Mar. Res.*, **3**, 51–75.
- St. Laurent, L., and R. W. Schmitt, 1999: The contribution of salt fingers to vertical mixing in the North Atlantic Tracer Release Experiment. *J. Phys. Oceanogr.*, **29**, 1404–1424.
- Stommel, H., and K. N. Fedorov, 1967: Small-scale structure in temperature and salinity near Timor and Mindanao. *Tellus*, **19**, 76–81.
- Stull, R. B., and E. B. Kraus, 1987: The transiient model of the upper ocean. *J. Geophys. Res.*, **92C**, 10 745–10 755.
- Tang, C. L., A. S. Bennett, and D. J. Lawrence, 1985: Thermohaline intrusions in the frontal zones of a warm-core ring observed by batfish. *J. Geophys. Res.*, **90C**, 8928–8942.
- Thomas, L. N., and C. M. Lee, 2005: Intensification of ocean fronts by down-front winds. *J. Phys. Oceanogr.*, **35**, 1086–1102.
- , A. Tandon, and A. Mahadevan, 2008: Sub-mesoscale processes and dynamics. *Ocean Modeling in an Eddying Regime, Geophys. Monogr.*, Vol. 177, Amer. Geophys. Union, 17–38.
- , C. M. Lee, and Y. Yoshikawa, 2010: The Subpolar Front of the Japan/East Sea. Part II: Inverse method for determining the frontal vertical circulation. *J. Phys. Oceanogr.*, **40**, 3–25.
- Turner, J. S., and C. F. Chen, 1974: Two-dimensional effects in double-diffusive convection. *J. Fluid Mech.*, **63**, 577–592.
- Wahba, G., and J. Wendelberger, 1980: Some new mathematical methods for variational objective analysis using splines and cross validation. *Mon. Wea. Rev.*, **108**, 1122–1143.
- Woods, J. D., R. Onken, and J. Fischer, 1986: Thermohaline intrusions created isopycnetically at oceanic fronts are inclined to isopycnals. *Nature*, **322**, 446–449.